JCB Journal of Cell Biology

ARTICLE

Homeostatic scaling of active zone scaffolds maintains global synaptic strength

Pragya Goel[1], Dominique Dufour Bergeron[2], Mathias A. Böhme[3], Luke Nunnelly[1], Martin Lehmann[4], Christopher Buser[5], Alexander M. Walter[3], Stephan J. Sigrist[2], and Dion Dickman[1]

Synaptic terminals grow and retract throughout life, yet synaptic strength is maintained within stable physiological ranges. To study this process, we investigated *Drosophila endophilin* (*endo*) mutants. Although active zone (AZ) number is doubled in *endo* mutants, a compensatory reduction in their size homeostatically adjusts global neurotransmitter output to maintain synaptic strength. We find an inverse adaptation in *rab3* mutants. Additional analyses using confocal, STED, and electron microscopy reveal a stoichiometric tuning of AZ scaffolds and nanoarchitecture. Axonal transport of synaptic cargo via the lysosomal kinesin adapter Arl8 regulates AZ abundance to modulate global synaptic output and sustain the homeostatic potentiation of neurotransmission. Finally, we find that this AZ scaling can interface with two independent homeostats, depression and potentiation, to remodel AZ structure and function, demonstrating a robust balancing of separate homeostatic adaptations. Thus, AZs are pliable substrates with elastic and modular nanostructures that can be dynamically sculpted to stabilize and tune both local and global synaptic strength.

Introduction

The astounding ability of synapses to change in both structure and function over time is well known. While this plasticity is necessary for development and experiential modification in the nervous system, this flexibility is also inherently destabilizing. When synapses are increased or reduced in number or strength, the balance between excitatory and inhibitory activity may be inappropriately weighted, leading to maladaptive changes in information transfer and circuit functionality (Turrigiano and Nelson, 2004; Yizhar et al., 2011; Landau et al., 2016). Indeed, chronic conditions of imbalance contribute to seizures, excitotoxicity, neuropsychiatric diseases, and neurodegeneration (Eichler and Meier, 2008; Nelson and Valakh, 2015; Hunt et al., 2017; Styr and Slutsky, 2018). Despite the diverse challenges that neurons, synapses, and circuits confront throughout development, maturation, aging, and disease, neural activity remains remarkably stable. These observations have inspired hypotheses that synapses are endowed with potent and adaptive homeostatic signaling systems that maintain stable functionality in response to these perturbations (Turrigiano et al., 1998; Turrigiano and Nelson, 2004; Pozo and Goda, 2010; Davis and Müller, 2015). Although it is now well established that individual synapses can undergo both Hebbian and homeostatic forms of plasticity (Pozo and Goda, 2010; Turrigiano, 2012; Davis, 2013; Herring and Nicoll, 2016; Keck et al., 2017), how global synaptic strength is stabilized and integrated with synapse-specific modulations remains enigmatic.

The *Drosophila melanogaster* neuromuscular junction (NMJ) is an ideal system to investigate the integration and stabilization of synaptic growth and function. At this model glutamatergic synapse, the NMJ expands over 100-fold during 5 d of larval development, maintaining stable muscle excitation despite the immense differences in the volume, architecture, and passive electrical properties of the muscle (Atwood et al., 1993; Schuster et al., 1996; Menon et al., 2013). Indeed, even at terminal stages, a broad variation in synaptic growth and number at the fly NMJ has been noted (Liebl et al., 2006; Menon et al., 2013; Goel et al., 2019a), yet global synaptic strength remains constrained within narrower physiological ranges (Broadie and Bate, 1995; Dickman and Davis, 2009; Rushton et al., 2009; Müller et al., 2011; Goel et al., 2019a). This stability persists even in manipulations that lead to NMJ overgrowth in extended larval stages (Miller et al., 2012). One of the most dramatic examples of global synaptic strength being stabilized in the face of synaptic overgrowth is illustrated in mutations of the endocytic gene *endophilin* (*endo*).

[1]Department of Neurobiology, University of Southern California, Los Angeles, CA; [2]Institute for Biology, Freie Universität Berlin, Berlin, Germany; [3]Neurocure Cluster of Excellence, Charité Universitätsmedizin, Berlin, Germany; [4]Leibniz-Forschungsinstitut für Molekulare Pharmakologie, Berlin, Germany; [5]Oak Crest Institute of Science, Monrovia, CA.

Correspondence to Dion Dickman: dickman@usc.edu.

endo mutants exhibit extreme synaptic overgrowth due to defective endocytic regulation of a growth-promoting signaling system (Dickman et al., 2006; O'Connor-Giles et al., 2008). In addition, synaptic vesicle (SV) size is enhanced and vesicle number reduced at *endo* mutant NMJs (Verstreken et al., 2002; Dickman et al., 2005). However, despite these challenges, baseline synaptic strength is maintained at wild-type levels in *endo* mutants (Verstreken et al., 2002; Dickman et al., 2005). Together, these findings imply the existence of a mechanism that tunes global neurotransmitter output to scale with synaptic growth and thus homeostatically stabilize overall synaptic strength at the NMJ.

Two independent homeostats stabilize synaptic strength at the *Drosophila* NMJ. First, presynaptic homeostatic potentiation (PHP) is expressed following genetic or pharmacological perturbations that diminish postsynaptic glutamate receptor functionality (Frank, 2014). In response, a retrograde signaling system from the muscle drives a precise enhancement in presynaptic glutamate release that maintains baseline levels of synaptic strength (Petersen et al., 1997; Frank et al., 2006). PHP can be induced at specific synapses in a target-specific manner, potentiating a subset of release sites within the terminal of a single neuron (Newman et al., 2017; Li et al., 2018a), suggesting PHP locally modulates the efficacy of neurotransmitter release. Second, presynaptic homeostatic depression (PHD) reduces neurotransmitter release in response to excess glutamate emitted from individual SVs, in effect maintaining stable synaptic strength (Daniels et al., 2004; Gaviño et al., 2015; Li et al., 2018b). Excess glutamate is released due to enlarged SV size, which can result from mutations that disrupt SV endocytosis (Verstreken et al., 2002; Koh et al., 2004; Marie et al., 2004; Dickman et al., 2005; Chen et al., 2014) or from neuronal overexpression of the vesicular glutamate transporter (vGlut-OE; Daniels et al., 2004). In either case, increased glutamate is emitted from individual vesicles, but a homeostatic reduction in the number of vesicles released per stimulus at each NMJ stabilizes synaptic strength (Daniels et al., 2004; Gaviño et al., 2015; Li et al., 2018b). Both PHP and PHD are latent forms of synaptic plasticity that do not typically function as part of normal development but are revealed as a response to specific challenges (glutamate receptor perturbation or excess glutamate release). Importantly, neither PHP nor PHD involve any major changes in synapse growth or number; rather, they are expressed through functional changes in presynaptic release probability (Daniels et al., 2004; Müller and Davis, 2012; Newman et al., 2017; Li et al., 2018b). Thus, while there is no evidence that PHP or PHD contributes to the stabilization of synaptic strength during NMJ growth and structural maturation (Dickman and Davis, 2009; Li et al., 2018b), homeostatic mechanisms must interface over chronic timescales with developmental signaling systems to ensure stable levels of neurotransmission.

We have investigated synaptic growth, structure, function, and plasticity in *endo* mutants to determine how synaptic strength across the entire NMJ is stabilized. This analysis has revealed that while the number of active zones (AZs) is dramatically increased in proportion to synaptic overgrowth in *endo* mutant NMJs, an adaptive reduction in the abundance of AZ components at individual release sites maintains global synaptic output. Furthermore, a similar scaling of AZ number and size is also observed in *rab3* mutants (Graf et al., 2009), where a reduction in AZ number is offset by a dramatic increase in the area of individual AZs. One important mechanism that controls the abundance of AZ material endowed at NMJs is mediated by axonal transport of synaptic cargo via the lysosomal kinesin adaptor Arl8. Finally, despite this homeostatic scaling of AZ structure, both *endo* and *rab3* mutants can undergo additional homeostatic modulations required to express PHD and PHP, independent forms of plasticity that target AZ structure and function. Hence, AZs are pliable nodes targeted by multiple plasticity signaling systems that are capable of being dynamically molded to tune both local and global synaptic strength.

Results

Stable synaptic strength is maintained at *endo* mutant NMJs despite enhanced synaptic growth and quantal size

To investigate how an extreme increase in synaptic growth and quantal size together impact synaptic function, we characterized *endo* mutants at the *Drosophila* NMJ. At this synapse, wild-type presynaptic terminals exhibit a characteristic morphology, with stereotyped numbers of synaptic boutons, protrusions of rounded morphology that are considered units of synaptic function (Atwood et al., 1993; Budnik et al., 1996; Schuster et al., 1996). This stereotyped morphology can be visualized by immunostaining the neuronal membrane as an array of ∼40 boutons/NMJ on muscle 4 (Fig. 1, A and B). Similarly, wild-type NMJs also have stereotyped levels of transmission, with consistent values of miniature excitatory postsynaptic potentials (mEPSPs), evoked responses (EPSP amplitude), and numbers of vesicles released per stimulus (quantal content; Fig. 1, C–F). In striking contrast, *endo* mutants exhibit dramatic increases in synaptic growth, including an ∼100% increase in the number of synaptic boutons (Fig. 1, A and B; Dickman et al., 2006). Further, *endo* NMJs have an ∼40% increase in quantal size (Fig. 1, C and E) due to enhanced SV size (Verstreken et al., 2002; Dickman et al., 2005). However, despite these changes in synaptic structure and vesicular glutamate emission, EPSP amplitudes are similar to wild-type (Fig. 1, C and D) due to a homeostatic reduction in quantal content (Fig. 1, F and G). Thus, *endo* NMJs express PHD to compensate for enhanced quantal size but must also undergo additional adaptive modulations to compensate for the dramatic synaptic overgrowth.

We included two important controls to establish in which compartment *endo* functions and to separate the modulations necessary for PHD expression from those required to adapt to synaptic overgrowth. First, the enhancement in quantal size could be due to a presynaptic function of *endo* (increased vesicle size) or, alternatively, a postsynaptic role of *endo* (such as enhanced glutamate receptor levels). To address this, we knocked down *endo* selectively in neurons (endo^{RNAi}) and restored *endo* expression in neurons at *endo* mutant NMJs (*endo* rescue). This showed that endo^{RNAi} phenocopied *endo* mutants, while *endo* rescue restored NMJ structure and mEPSP amplitude (Fig. 1, A–F), demonstrating *endo* has functions presynaptically to

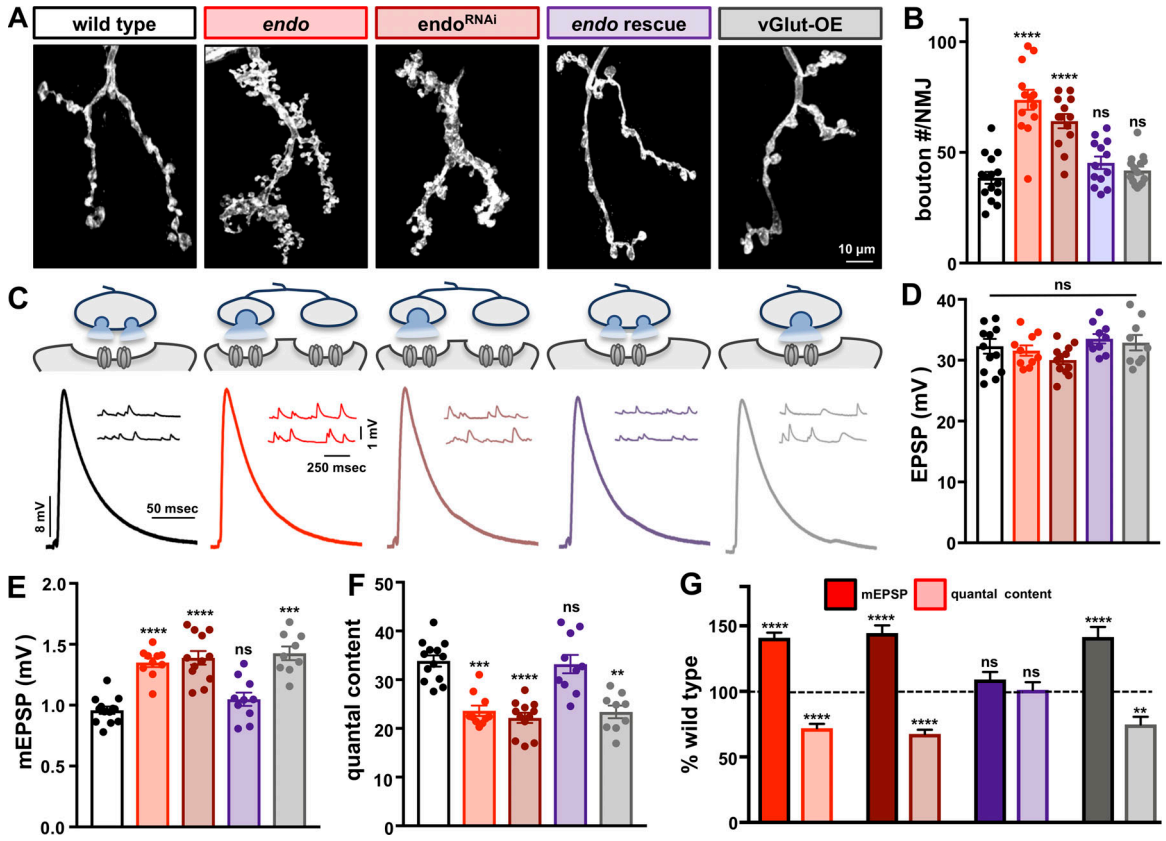

Figure 1. **Synaptic strength is stabilized despite enhanced synaptic growth and quantal size in *endo* mutants. (A)** Representative images of third-instar larval muscle 4 NMJs immunostained with antibodies against the neuronal membrane marker HRP. Wild-type NMJs (w^{1118}) serve as the control condition. *endo* mutants (*endo: w;endo*^{1}*/endo*$^{\Delta 4}$) and neuronal knockdown of *endo* (endo^{RNAi}: *w;OK6-Gal4;UAS-endo-RNAi*) result in synaptic overgrowth. Neuronal expression of *endo* in *endo* mutant backgrounds (*endo* rescue: *c155-Gal4;+;endo*^{1}) rescues the synaptic overgrowth phenotype. Presynaptic overexpression of *vGlut* (vGlut-OE: *w;OK371-Gal4/UAS-vGlut*) shows no significant change in synaptic growth. **(B)** The number of synaptic boutons, a measure of synaptic growth, is significantly increased in *endo* and endo^{RNAi} ($n \geq 13$; one-way ANOVA; Table S1). **(C)** Schematic and representative electrophysiological traces in the indicated genotypes. Neurotransmitter released by SVs is meant to illustrate evoked release. In addition to increased bouton number in *endo*, note the increased vesicle size schematized in *endo*, endo^{RNAi}, and vGlut-OE, which induces PHD. **(D–E)** mEPSP amplitudes are significantly increased in *endo*, endo^{RNAi}, and vGlut-OE (E), while EPSP amplitudes remain unchanged compared with wild type (D), leading to a homeostatic reduction in presynaptic neurotransmitter release (quantal content; F). **(G)** Quantification of mEPSP amplitude and quantal content, normalized to wild-type values, demonstrates PHD in *endo*, endo^{RNAi}, and vGlut-OE, with increased mEPSP amplitude but a compensatory reduction in quantal content. Error bars indicate ± SEM ($n \geq 9$; one-way ANOVA; Table S1). **, $P < 0.01$; ***, $P < 0.001$; ****, $P < 0.0001$; ns, not significant.

control synaptic growth and vesicle size (Fig. 1, A–F), in agreement with previous studies (Verstreken et al., 2002; Dickman et al., 2005, 2006). Second, to control for PHD expression independently of altered synaptic growth, we examined vGlut-OE NMJs. vGlut-OE expressed PHD (Fig. 1, C–G) with no significant differences in synaptic growth (Fig. 1, A and B). Together, this demonstrates that PHD expression itself does not alter synaptic growth and that *endo* NMJs must use additional homeostatic mechanisms to compensate for synaptic overgrowth, separate from PHD expression, to maintain stable synaptic strength.

Although *endo* and vGlut-OE synapses differ dramatically in terms of synaptic growth and morphology, they appear electrophysiologically identical (Fig. 1). While both conditions have been shown to enlarge SV size (Verstreken et al., 2002; Daniels et al., 2004; Dickman et al., 2005), it is unclear whether distinct or shared mechanisms are involved. First, we quantified SV size directly in both *endo* and vGlut-OE using EM. This confirmed that both genotypes exhibit increased SV diameter (Fig. S1, A, B, and D), as previously reported (Verstreken et al., 2002; Daniels et al., 2004; Dickman et al., 2005). In addition, SV density was reduced by ∼80% in *endo*, but no change was found in vGlut-OE (Fig. S1, A and C). The reduction in SV number in *endo* mutants was previously observed (Verstreken et al., 2002; Dickman et al., 2005) and interpreted to result from defective endocytosis and vesicle reformation mechanisms. In contrast, vGlut-OE does not change the total number of releasable SVs (Li et al., 2018b) but does enhance vesicle size through increased expression of *vGlut* (Daniels et al., 2004). We quantified fluorescence intensity levels of individual vGlut puncta and found the expected increase in mean puncta intensity in vGlut-OE, but we observed no change in *endo* (Fig. S1, E and F). In addition, enhanced *vGlut* expression did not change levels of other SV markers, Synapsin and Synaptotagmin, which were similar between wild type, *endo*, and vGlut-OE (Fig. S1, E and F). This suggests that the enlarged vesicle size observed in *endo* does not involve the same increased *vGlut* expression mechanism found

in vGlut-OE. Finally, high-frequency stimulation of *endo* NMJs leads to a rapid rundown of the vesicle pool, indicative of defective SV endocytosis (Verstreken et al., 2002; Dickman et al., 2005). However, when vGlut-OE NMJs were subjected to this protocol, we found the vesicle pool was effectively sustained (Fig. S2). Therefore, distinct mechanisms enlarge vesicle size at *endo* and vGlut-OE synapses, while both express PHD, consistent with excess glutamate emitted per vesicle being the key perturbation necessary to induce this form of homeostatic plasticity (Daniels et al., 2004; Li et al., 2018b).

Increased Bruchpilot (BRP) puncta number but reduced puncta area at *endo* NMJs

endo and vGlut-OE NMJs both express PHD, but *endo* mutants maintain stable synaptic strength despite a dramatic increase in NMJ growth. Because mEPSP amplitude and quantal content are similar between *endo* and vGlut-OE, a change in the number and/or release probability of individual synapses must have occurred in *endo*. Indeed, the increase in NMJ growth in *endo* would be expected to increase EPSP amplitude and quantal content if all other functional parameters remained constant. Although bouton number was increased in *endo*, the size of individual boutons appeared smaller (Fig. 1, A and B), so we first determined whether total neuronal membrane area scaled with NMJ growth. This analysis showed that while the size of individual boutons was indeed smaller in *endo* and endo^{RNAi} compared with wild type (Table S1), *endo* mutants still exhibited an ∼100% increase in neuronal membrane surface area (Fig. 2 B). No changes in neuronal membrane surface area were observed in *endo* rescue and vGlut-OE (Fig. 2 B). Thus, neuronal membrane area scales with NMJ growth at *endo* NMJs.

Next, we considered that while *endo* mutants may exhibit enhanced bouton number and neuronal membrane surface area, perhaps the density of AZs was reduced to preserve similar overall number of release sites compared with wild type. To identify individual AZs, we immunostained NMJs using an antibody that recognizes BRP, a central scaffold that constitutes the "T-bar" structure at the center of the AZ (Kittel et al., 2006; Wagh et al., 2006). We defined a BRP punctum as an AZ, as ∼96% of AZs at the fly NMJ are labeled by BRP (Wagh et al., 2006), and those AZs that are devoid of BRP appear to play minimal to noncontributing roles in neurotransmission (Graf et al., 2009; Akbergenova et al., 2018). While *endo* rescue and vGlut-OE had similar densities and total numbers of BRP puncta per NMJ compared with wild type, both *endo* and endo^{RNAi} had normal BRP puncta density, resulting in a concomitant increase in the total BRP puncta number per NMJ that scaled with neuronal membrane and bouton numbers (Fig. 2, A, C, and D). Thus, *endo* mutants have enhanced numbers of release sites in proportion to synaptic growth, suggesting a change in release probability per AZ must have occurred to stabilize synaptic strength.

Finally, we considered whether a change in the size of individual BRP puncta might have contributed to the homeostatic control of neurotransmission (EPSP amplitude) in *endo* mutants. Several studies have shown that the abundance of material at AZs, reflected in their intensity, area, and/or nanoarchitecture, change during various forms of plasticity, which positively correlate with release probability (Ehmann et al., 2014; Glebov et al., 2017; Akbergenova et al., 2018; Dong et al., 2018; Li et al., 2018b; Böhme et al., 2019; Gratz et al., 2019; Lübbert et al., 2019). For example, increased AZ size reflected by enhanced BRP puncta area at individual AZs permits more fusion-ready SVs and calcium channels to enhance release probability (Graf et al., 2009; Matkovic et al., 2013; Akbergenova et al., 2018; Gratz et al., 2019). We therefore quantified the area of individual BRP puncta and observed an ∼35% decrease in *endo* compared with wild type (Fig. 2, A and E). PHD expression does not contribute to this change in AZ size, as BRP puncta area in vGlut-OE was unchanged compared with wild type (Fig. 2, A and E). Interestingly, the structure of postsynaptic glutamate receptors mirrored presynaptic structure at *endo* NMJs, with an increased number, no change in density, and reduced size of GluRIII puncta (Fig. S3, A–C). Remarkably, *endo* NMJs remained highly organized in structure, with normal AZ/receptor apposition (Fig. S3, A and E). Similar changes in BRP puncta size were observed in endo^{RNAi} and restored to wild-type values in *endo* rescue (Fig. 2, A–E; and Fig. S3, A–E). This suggests that the size of individual BRP puncta may have been scaled to reduce release probability and offset the increased number of release sites in *endo* mutants.

Scaling of BRP puncta size and number is also observed when AZ density is reduced in *rab3* mutants

Given the changes in BRP puncta number and size observed in *endo* mutants, we next characterized these properties in *rab3* mutants, which exhibit unperturbed NMJ growth but reduced density of AZs. Rab3 is a small GTPase proposed to subserve an important role in controlling the genesis, spacing, and/or nucleation sites of AZs (Graf et al., 2009). Mutations in *Drosophila rab3* were identified in a forward genetic screen, where a striking change in AZ structure was discovered (Graf et al., 2009). In particular, *rab3* mutants have a threefold reduction in the density of BRP puncta and no change in bouton number or neuronal membrane surface area compared with wild type, which we confirmed (Fig. 3, A–C; and Table S1; Graf et al., 2009). This decrease in BRP puncta density results in a reduction in the total number of BRP puncta per NMJ (Fig. 3, A and F; Graf et al., 2009). However, despite the reduction in the total number of BRP puncta, EPSP amplitude remains similar in *rab3* mutants compared with wild type (Graf et al., 2009), which we confirmed (Fig. 3, D and E). We measured the size of individual BRP puncta in *rab3* mutants and found a significantly increased area (Fig. 3 G). Thus, *rab3* mutants show inverse changes in the size of individual BRP puncta as well as the total number per NMJ compared with *endo* mutants.

Homeostatic scaling of quantal content as a function of mEPSP amplitude has been observed to maintain synaptic strength in both PHP and PHD (Frank et al., 2006; Gaviño et al., 2015; Li et al., 2018b). We considered that if AZ scaling were truly homeostatic, then BRP puncta size should scale with the total number of BRP puncta per NMJ across wild type, *endo*, and *rab3* mutants. We therefore plotted average BRP puncta area against average BRP puncta number per NMJ in these genotypes. We found that BRP puncta area indeed inversely scales with total

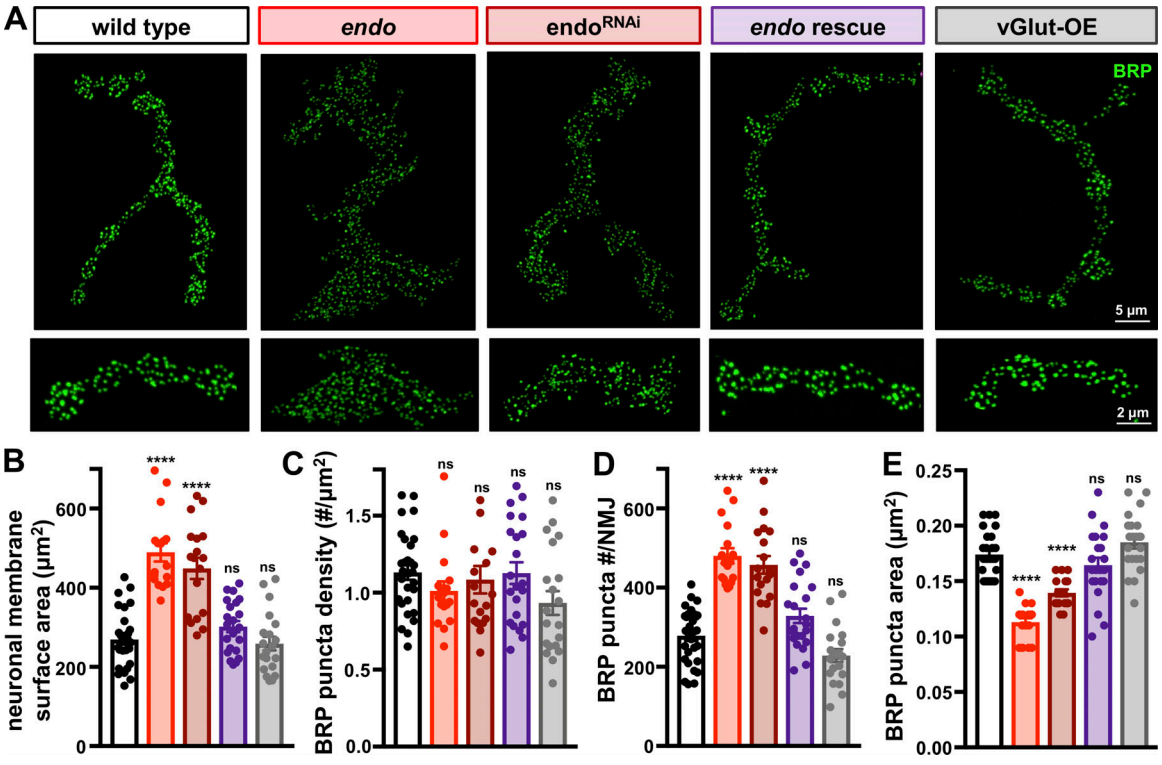

Figure 2. **Increased AZ number but reduced AZ size revealed at *endo* mutant NMJs. (A)** Representative NMJs in the indicated genotypes immunostained with antibodies against the AZ protein BRP, with insets below showing individual boutons from the same NMJ. **(B)** Quantification of neuronal membrane surface area (labeled by HRP) shows a significant increase in *endo* and endo^{RNAi}, which is rescued in *endo* rescue with no change found in vGlut-OE. **(C)** No change in BRP puncta density is observed in any genotype. **(D)** Total BRP puncta number per NMJ is significantly increased in *endo* and endo^{RNAi}, which scales with the increased neuronal membrane surface area. **(E)** A significant reduction in the area of individual BRP puncta is observed in *endo* and endo^{RNAi}, while no significant change is found in vGlut-OE. Error bars indicate ± SEM ($n \geq 17$; one-way ANOVA; Table S1). ****, $P < 0.0001$; ns, not significant.

BRP puncta number per NMJ in wild type, *endo*, endo^{RNAi}, *rab3*, and vGlut-OE, falling along an idealized tuning curve (Fig. 3 H), akin to the homeostatic scaling of quantal content with mEPSP amplitude. Thus, BRP puncta area scales with the number of BRP puncta per NMJ.

If *endo* and *rab3* modulate AZ size and number through the same genetic pathway, then the AZ phenotype observed in one of these mutants should be epistatic to the other. However, if AZ size and number are modulated independently of *endo* or *rab3* function (e.g., in response to increased neuronal membrane surface area or AZ density alone), then a combination of these genetic mutations should result in a phenotype intermediate to either mutant alone. We therefore assessed BRP puncta size and number when loss of *endo* is combined with loss of *rab3* at an NMJ. In *rab3;endo* double mutants, we observed a small increase in membrane surface area but no significant difference in BRP puncta density (Fig. 3, A–C). Interestingly, a small increase in the total number of BRP puncta per NMJ was observed in *rab3;endo* double mutants, with no significant difference in BRP puncta area compared with wild type (Fig. 3, F and G). Importantly, a similar scaling of BRP puncta size with number was found in *rab3;endo* double mutants compared with wild type (Fig. 3 H), which also stabilized synaptic strength to levels unchanged from wild type (Fig. 3, D and E). Thus, BRP puncta size is inversely tuned with total BRP puncta number per NMJ, while synaptic strength remains constant across NMJs from wild type, *endo*, *rab3*, vGlut-OE, and *rab3;endo* mutants. This indicates that perturbations to membrane surface area or AZ density, and not PHD expression, adaptively modulate AZ size to stabilize global neurotransmitter output at the NMJ.

Total BRP, Unc13A, and Ca^{2+} channel abundance is conserved across wild-type, *endo*, and *rab3* mutant NMJs

How might reciprocal changes in BRP puncta number and area ensure stable levels of global synaptic strength? BRP anchors voltage gated Ca^{2+} channels at release sites and controls the size of the readily releasable vesicle pool (Kittel et al., 2006; Matkovic et al., 2013). BRP also stabilizes Unc13A, an AZ scaffold that controls release site number, position, and functionality (Böhme et al., 2016; Reddy-Alla et al., 2017). A change in the abundance of BRP and/or Unc13A could, in principle, bidirectionally modulate the probability of release at individual AZs. First, we characterized the mean intensity of BRP at individual puncta (BRP mean intensity) and found no significant difference compared with wild type in *endo* and vGlut-OE (Fig. 4, A and B). A slight but significant increase was observed in *rab3* mutants, suggesting a mild increase in the density of BRP protein at these large AZs, as previously noted (Graf et al., 2009). However, the sum intensity of individual BRP puncta (BRP sum intensity) was

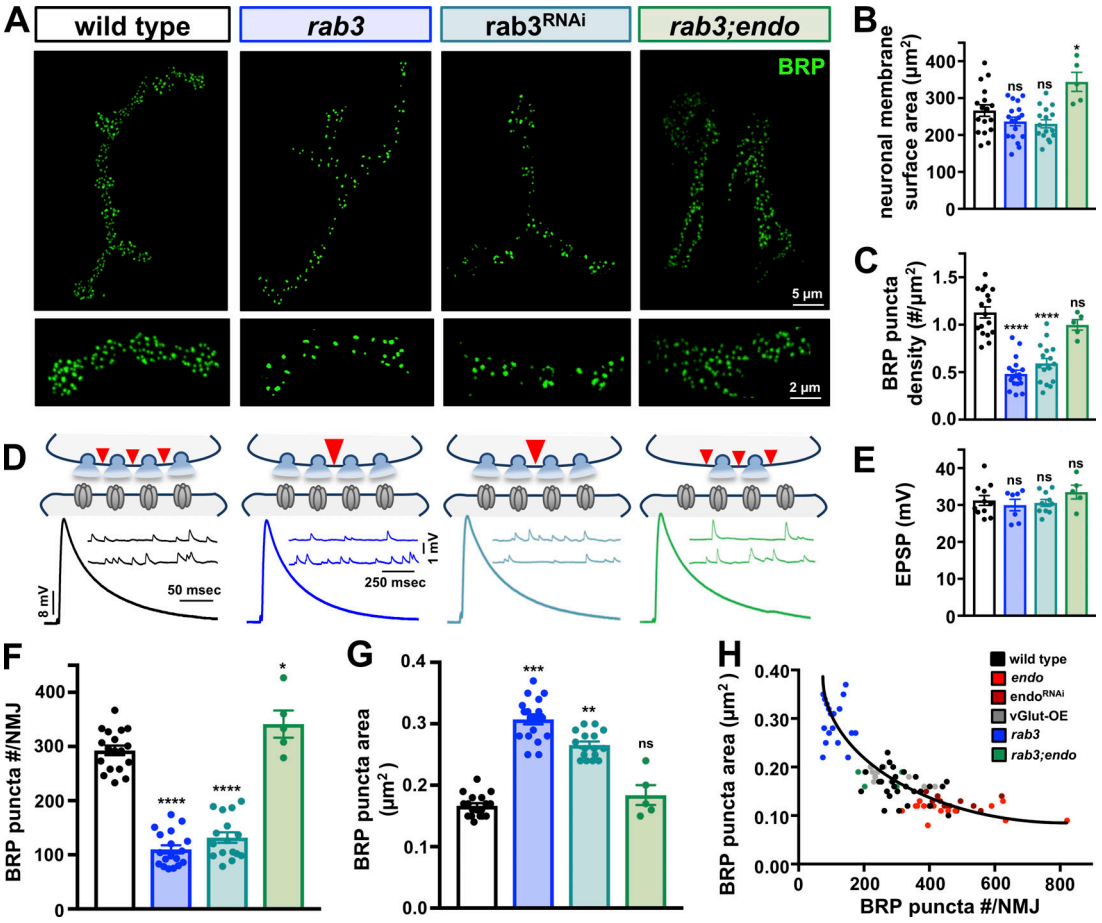

Figure 3. **Increased AZ size but reduced number and density at *rab3* mutant NMJs. (A)** Representative NMJs immunostained with anti-BRP and insets below showing individual boutons from the same NMJ in wild-type, *rab3* mutants (*w;rab3^{rup}*), neuronal knockdown of *rab3* (rab3^{RNAi}: *c155-Gal4;+;UAS-rab3-RNAi/+*), and *rab3;endo* double mutants (*w;rab3^{rup};endo^{1}/endo$^{\Delta 4}$*). **(B)** No change in neuronal membrane surface area is observed in *rab3* mutants and rab3^{RNAi}, while a small but significant increase is found in *rab3;endo* double mutants. **(C)** BRP puncta density is significantly reduced in *rab3* and rab3^{RNAi} but is unchanged in *rab3;endo* double mutants. **(D)** Schematic and representative traces of AZ size, density, and neurotransmitter release at NMJs of the indicated genotypes, with no significant difference in EPSP amplitude observed **(E)**. **(F and G)** *rab3* mutants and rab3^{RNAi} show a significant reduction in the total number of BRP puncta per NMJ (F), but exhibit an increase in the area of individual BRP puncta (G); these values are similar to wild type in *rab3;endo*. **(H)** A homeostatic tuning is observed where BRP puncta area scales with total BRP puncta number per NMJ in all genotypes. The black curve represents ideal homeostatic tuning with a goodness of fit R^2 value of 0.729. Error bars indicate ± SEM ($n \geq 5$; one-way ANOVA; Table S1). *, P < 0.05; **, P < 0.01; ***, P < 0.001; ****, P < 0.0001; ns, not significant.

decreased in *endo*, increased in *rab3* mutants, and unchanged in vGlut-OE (Fig. 4, A and C), consistent with the observed changes in BRP puncta size. Next, we analyzed the level of Unc13A puncta at AZs. As with BRP puncta, we found no significant difference in the mean intensity of Unc13A localized with individual BRP puncta (Unc13A mean intensity) but opposing changes in sum Unc13A intensity per BRP puncta in *endo* and *rab3* mutants (Fig. 4, A–C), consistent with decreased and increased AZ size. Finally, we analyzed the level of the CaV2.1 Ca^{2+} channel Cacophony (Cac) using an endogenously tagged channel (Cac$^{sfGFP\text{-}N}$) recently developed (Gratz et al., 2019). A previous study proposed that PHD homeostatically reduces the abundance of overexpressed Cac-GFP at AZs, where reduced intensity of the tagged UAS-Cac-GFP channel was observed in vGlut-OE (Gaviño et al., 2015). However, the abundance of Cac$^{sfGFP\text{-}N}$ does not change in vGlut-OE (Gratz et al., 2019), which we confirmed (Fig. 4, A–C). As with BRP and Unc13A puncta size, we observed no significant difference in the mean intensity of Cac localized within individual BRP puncta (Cac mean intensity) but opposing changes in sum Cac intensity per BRP puncta in *endo* and *rab3* mutants (Fig. 4, A–C), consistent with decreased and increased AZ size. Thus, the total abundance of BRP at individual AZs (BRP sum intensity) scales with Unc13A and Cac sum intensity, consistent with bidirectional control of release probability at individual AZs.

The bidirectional changes in BRP, Unc13A, and Cac puncta sum intensity, with no change in mean intensity, in *endo* and *rab3* mutants suggests that the density of these components at individual AZs was similar in both mutants, with the area occupied by these scaffolds explaining the apparent change in size and sum fluorescence intensity. Given that synaptic strength is similarly maintained across all conditions, we hypothesized that the total abundance of BRP, Unc13A, and Cac at NMJ terminals, independent of the size or number of individual puncta, may be

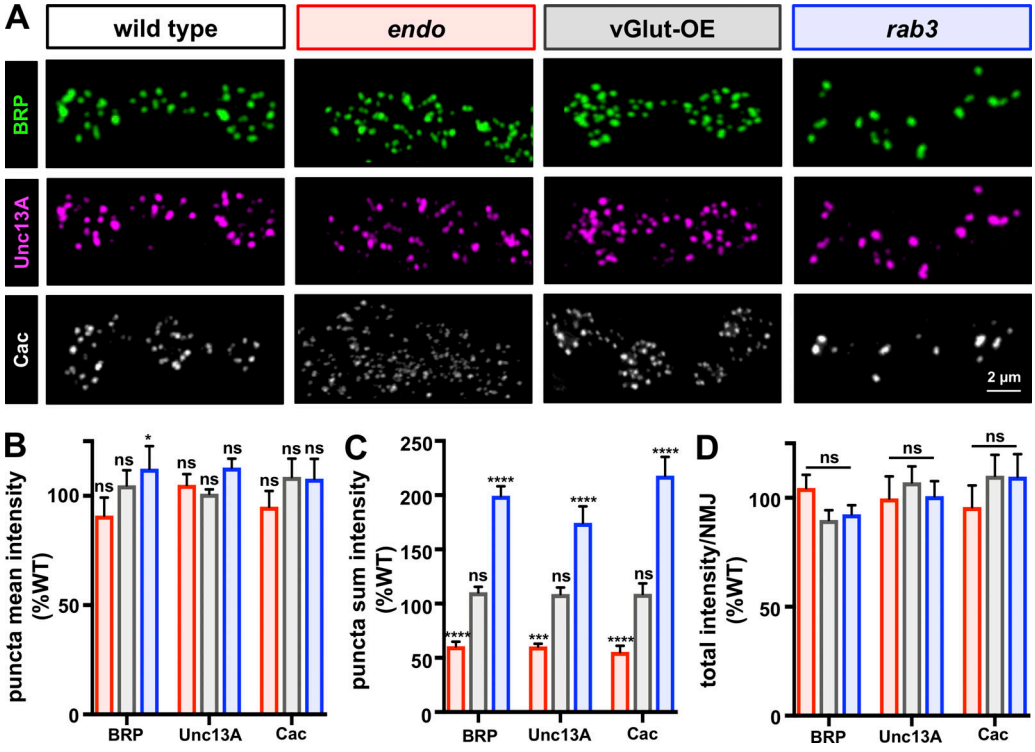

Figure 4. **BRP, Unc13A, and Cac abundance scale in *endo* and *rab3* mutants, while total levels per NMJ remain constant. (A)** Representative type Ib boutons immunostained with anti-BRP, anti-Unc13A, and endogenously tagged Ca^{2+} channels ($Cac^{sfGFP\text{-}N}$) in the indicated genotypes (wild type: $cac^{sfGFP\text{-}N}$; *endo*: $cac^{sfGFP\text{-}N}$;$endo^{1}/endo^{\Delta 4}$; vGlut-OE: $cac^{sfGFP\text{-}N}$;*OK371-Gal4/UAS-vGlut*; *rab3*: $cac^{sfGFP\text{-}N}$;$rab3^{rup}$). Note that BRP and Unc13A are costained at the same NMJ, while Cac images were acquired from a different NMJ of the same genotype. **(B)** Quantification of mean fluorescence intensity of individual BRP, Unc13A, and $Cac^{sfGFP\text{-}N}$ puncta shows no change in *endo* and vGlut-OE, with a slight but significant increase in *rab3*, consistent with no major difference in the density of material within each punctum. **(C)** Quantification of BRP, Unc13A, and $Cac^{sfGFP\text{-}N}$ puncta sum fluorescence intensity reveals a significant reduction in *endo*, an increase in *rab3*, and no change in vGlut-OE, consistent with the observed changes in puncta area for each genotype ($n \geq 15$; one-way ANOVA; Table S1). **(D)** The total fluorescence intensity of each individual BRP, Unc13A, and $Cac^{sfGFP\text{-}N}$ puncta summed across the entire muscle 4 NMJ terminal is unchanged in *endo*, *rab3*, and vGlut-OE compared with wild type. Error bars indicate ± SEM ($n \geq 8$; one-way ANOVA; Table S1). *, $P < 0.05$; ***, $P < 0.001$; ****, $P < 0.0001$; ns, not significant. See Materials and methods for more details on mean, sum, and total intensity measurements.

a major determinant of global presynaptic release probability across the entire NMJ. In this model, global synaptic output (glutamate release) is in effect tuned up or down at individual AZs at an inverse relationship with the total number of AZs per NMJ. Indeed, we found no significant difference in the total integrated fluorescence intensity of BRP, Unc13A, or Cac at entire NMJs between wild type, *endo*, *rab3*, and vGlut-OE (Fig. 4 D). Thus, while the abundance of key AZ components are sculpted in opposing directions at individual release sites at *endo* and *rab3* NMJs, as is the net number of AZs per NMJ, total levels of BRP, Unc13A, and Cac remain similar between wild type, *endo*, and *rab3*, as does synaptic strength.

stimulated emission depletion (STED) microscopy reveals a modular and elastic AZ nanostructure

Thus far we have used confocal microscopy to characterize AZ number and structure at the NMJ. While this approach offers a global analysis of hundreds of AZ puncta at single NMJs and provides an estimate of relative differences in their area, the limits of confocal resolution preclude an assessment of the architecture at individual AZs. However, STED microscopy offers superior resolution of up to ∼40 nm and has been used to unlock fundamental features about AZ nanoarchitecture at synapses (Kittel et al., 2006; Maglione and Sigrist, 2013; Hruska et al., 2018; Böhme et al., 2019). We therefore turned to STED imaging approaches to interrogate AZ nanostructure in *endo* and *rab3* mutants.

First, we analyzed the ring diameter of BRP and Unc13A at individual AZs in $endo^{RNAi}$ and *rab3* mutants. This analysis revealed an ∼35% reduction in the ring diameter of both BRP and Unc13A at individual AZs in $endo^{RNAi}$ and ∼100% increase in this diameter in *rab3* mutants (Fig. 5, A–C). Despite this reduction or enhancement of individual AZ diameter, we found the ratio of BRP:Unc13A was preserved across wild type, $endo^{RNAi}$, and *rab3* (Fig. 5 D), suggesting a stoichiometric balancing of these key AZ components that scale with AZ size. A previous study used EM analysis of AZs in *rab3* mutants to demonstrate that while the length of individual AZs was not significantly altered, there was an increase in the number of T bar structures per AZ (Graf et al., 2009). EM analysis of $endo^{RNAi}$ showed a reduction in both the length of AZs and the width of T bar structures (Fig. S4). However, AZ length and T bar structure were unchanged in vGlut-OE compared with wild type (Fig. S4), suggesting that AZ scaling, and not PHD

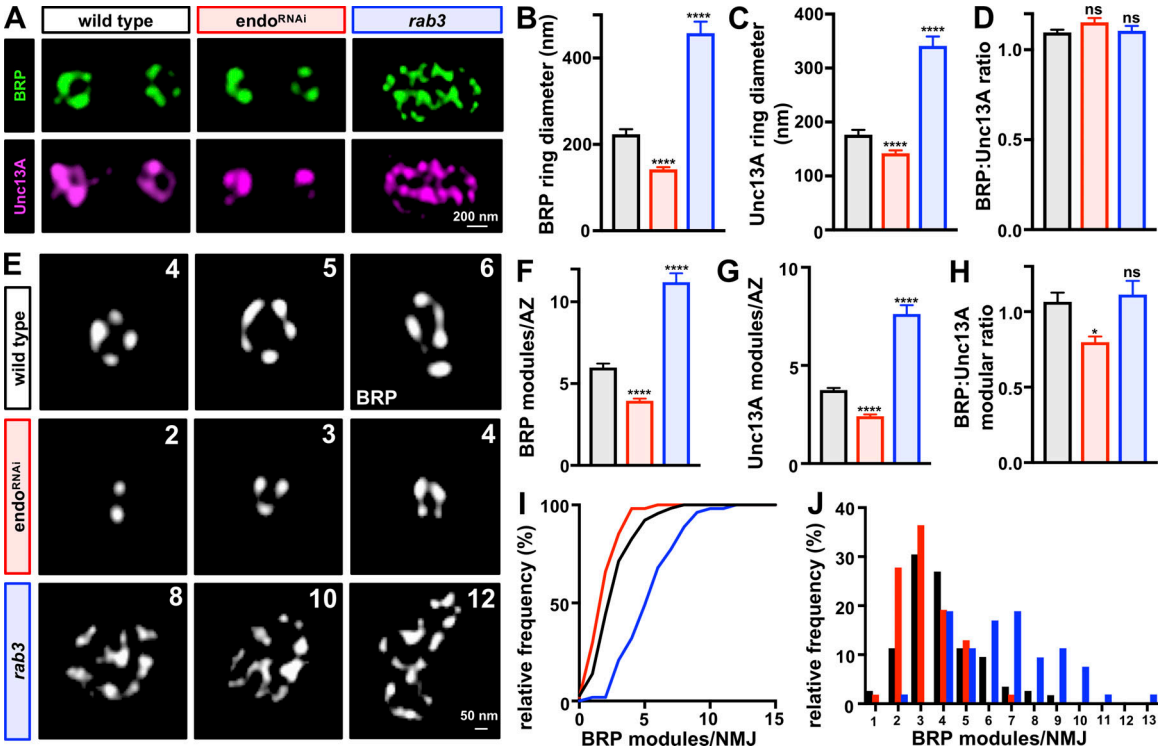

Figure 5. **Elastic modularity of AZ nanostructure revealed by STED imaging. (A)** Representative STED images of AZs in wild-type, endo^{RNAi}, and *rab3* mutant NMJs labeled with anti-BRP and anti-Unc13A. **(B–D)** BRP (B) and Unc13A (C) ring diameters are reduced in endo^{RNAi} and enhanced in *rab3* mutants, while the BRP:Unc13A ratio remains the same (D). **(E)** Quantal modules of BRP clusters within single AZs are revealed by STED analysis using an averaging algorithm (Böhme et al., 2019). The three modules of peak frequency are shown for wild type (4, 5, and 6 modules), endo^{RNAi} (2, 3, and 4), and *rab3* (8, 10, and 12). **(F–H)** Quantification of the mean number of BRP (F) and Unc13A (G) modules per AZ is shown, with a reduction in endo^{RNAi} and enhancement in *rab3*, while the ratio is largely unchanged (H). **(I and J)** Cumulative probability curve (I) and binned histogram (J) of BRP modules per NMJ are shown, with a leftward distribution observed in endo^{RNAi} and rightward shift in *rab3* mutants. Error bars indicate ± SEM ($n \geq 53$; one-way ANOVA, K-S test for I; Table S1). *, $P < 0.05$; ****, $P < 0.0001$; ns, not significant.

expression, controlled these features of AZ architecture in *endo*. Taken together, both STED and EM analysis demonstrate that the area of individual AZ structures can be bidirectionally modulated, while the relative levels of AZ components at individual release sites remain constant.

We next examined the modularity of AZ nanoarchitecture. We developed an algorithm to define local intensity maxima by determining the brightest pixel clusters with AZ domains measured by STED microscopy (see Materials and methods and Böhme et al., 2019). We leveraged this approach to reveal modular nanodomains of AZ components clustered within individual release sites. At wild-type AZs, we observed a Gaussian distribution of peak BRP and Unc13A modular intensities, with peak frequencies between 4 and 6 quanta per AZ (Fig. 5, E–G). This suggests that BRP and Unc13A are organized within distinct nanomodules at individual AZs and exhibit an average of 5–6 quantal units per AZ (Fig. 5, F–J). In contrast, a similar analysis of endo^{RNAi} revealed frequency peaks of 2–4 quanta and a remarkable 8–12 quanta in *rab3* mutants (Fig. 5, E–J). Thus, STED imaging and analysis highlights the striking elasticity that calibrates AZ nanoarchitecture, with quantal nanomodules increasing or decreasing in number at single AZs in an inverse relationship with the total number of AZs per NMJ.

Manipulating the abundance of AZ proteins at NMJs through *arl8*-dependent axonal transport bidirectionally adjusts synaptic strength

Thus far, we have shown that despite the changes in AZ size, intensity, and density between wild type, *endo*, and *rab3*, global synaptic strength and the total intensity of AZ components per NMJ remains constant. We considered, therefore, that perhaps the total abundance of AZ material at NMJs contributes toward setting the overall gain of neurotransmitter output. Recently, the lysosomal kinesin adaptor Arl8 was shown to control the delivery of presynaptic cargo to synaptic terminals via axonal transport (Vukoja et al., 2018). In particular, AZ components were cotransported with SV components through lysosome-related organelles to presynaptic NMJ terminals via Arl8. Loss of *arl8* reduced the total abundance of AZ and SV components at NMJs, with a concomitant reduction in evoked amplitude observed (Vukoja et al., 2018). Conversely, neuronal overexpression of *arl8* (arl8-OE) enhanced the abundance of AZ and SV material at NMJ terminals as well as global neurotransmitter release and synaptic strength. We sought to use *arl8* mutants and arl8-OE to manipulate the abundance of synaptic material at *endo* and *rab3* mutant NMJs and test whether global synaptic strength is similarly modulated.

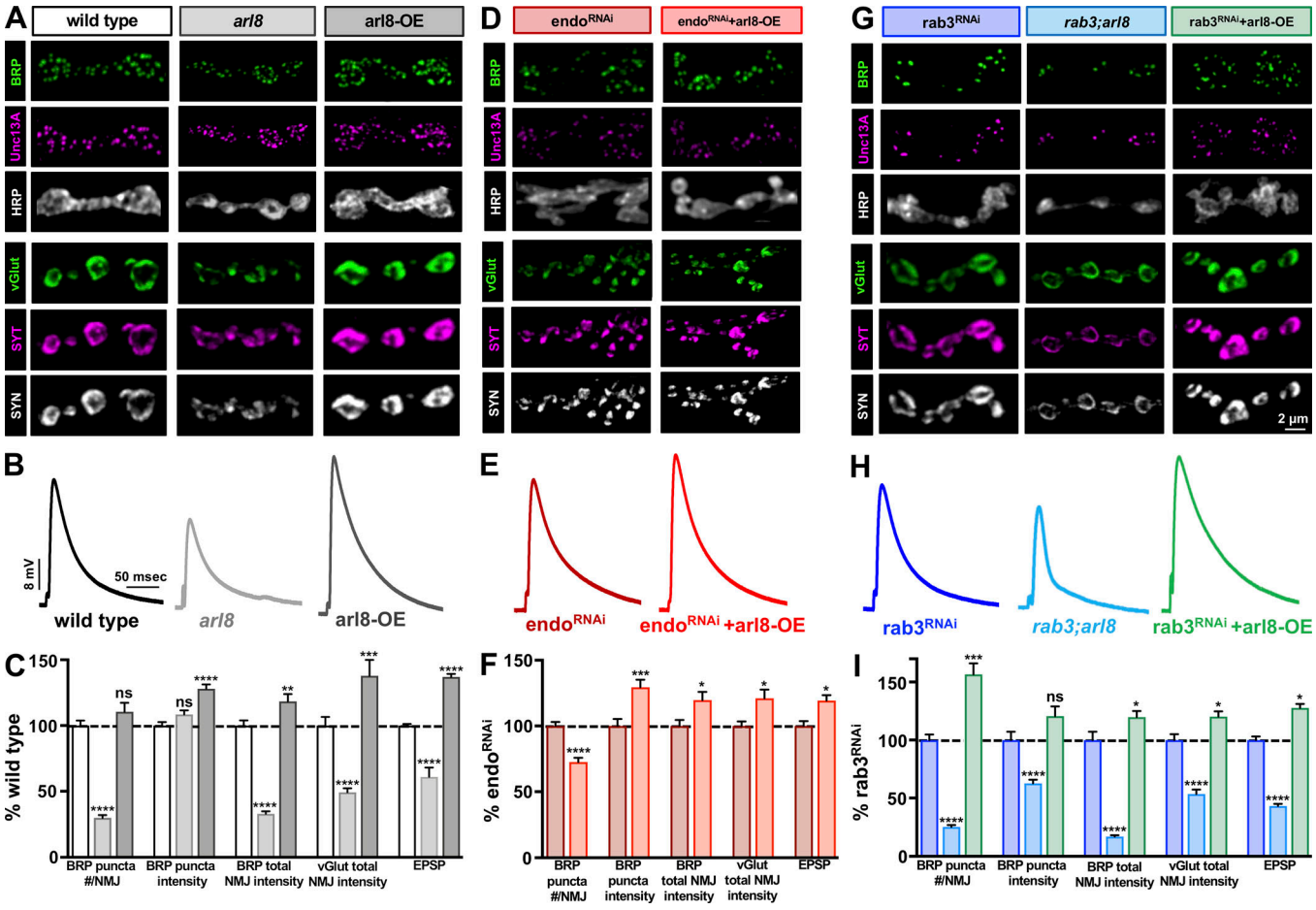

Figure 6. **Manipulating presynaptic cargo transport to NMJ terminals by *arl8* modulates the gain of synaptic strength at *endo* and *rab3* NMJs. (A)** Representative images of type Ib NMJ boutons immunostained with antibodies that recognize AZ components (BRP, Unc13A), neuronal membrane (HRP), and SV markers (vGlut, Synaptotagmin [SYT], and Synapsin [SYN]) in wild type, *arl8* mutants (*arl8*: *w;arl8^{e00336}*), and neuronal overexpression of *arl8* (arl8-OE: *w; OK6-Gal4,UAS-arl8-GFP/+*). Note that the number of AZs and the intensity of SV markers at NMJ terminals are reduced by loss of *arl8* (C; Table S1), while arl8-OE enhances the intensity of AZ and SV markers (C; Table S1). **(B)** EPSP traces in the indicated genotypes demonstrate that synaptic strength is reduced by loss of *arl8* and increased by arl8-OE. **(C)** Quantification of the indicated values in the three genotypes normalized to wild-type values ($n \geq 12$; one-way ANOVA; Table S1). **(D–F)** Representative images (D), EPSP traces (E), and quantification (F) for NMJs of endo^{RNAi} and endo^{RNAi} combined with arl8-OE (endo^{RNAi}+arl8-OE: *w;OK6-Gal4,UAS-arl8-GFP/+;UAS-endo-RNAi*). arl8-OE enhances synaptic strength and BRP and vGlut intensity above endo^{RNAi} baseline values (note that values are normalized to endo^{RNAi}; $n \geq 7$; Student's *t* test; Table S1). **(G–I)** Representative images (G), EPSP traces (H), and quantification (I) for NMJs of rab3^{RNAi}, *rab3*, and *arl8* double mutants (*rab3;arl8*: *w;rab3^{rup};arl8^{e00336}*), and rab3^{RNAi} combined with arl8-OE: rab3^{RNAi}+arl8-OE: *w;OK6-Gal4,UAS-arl8-GFP/+;UAS-rab3-RNAi*). Note that loss of *arl8* reduces BRP puncta number and intensities of BRP and vGlut below rab3^{RNAi} baseline values, while arl8-OE enhances these values. Values are normalized to rab3^{RNAi} ($n \geq 9$; one-way ANOVA; Table S1). Error bars indicate ± SEM. *, P < 0.05; **, P < 0.01; ***, P < 0.001; ****, P < 0.0001; ns, not significant.

First, we immunostained NMJs of wild type, *arl8* mutants, and arl8-OE to determine levels of AZ and SV components. As reported previously, we found that loss of *arl8* reduced total NMJ intensity of AZ (BRP and Unc13A) and SV components (vGlut, Synaptotagmin, and Synapsin), while arl8-OE increased their abundance (Fig. 6, A and C; and Table S1). As expected, this reduced EPSP amplitude in *arl8* and increased it in arl8-OE (Fig. 6, A–C). Next, we probed the impact of these manipulations on *endo* and *rab3*. Unfortunately, *arl8,endo* double mutants were lethal and did not survive to third-instar stages. However, arl8-OE combined with endo^{RNAi} increased BRP and vGlut puncta intensity and enhanced the abundance of AZ and SV proteins at NMJs, with a concomitant increase in synaptic strength (Fig. 6, D–F; and Table S1). Similarly, *rab3;arl8* double mutants reduced BRP puncta number and intensity, as well as AZ and SV abundance at NMJs, while reducing synaptic strength, and an inverse effect was observed at *rab3*+arl8-OE NMJs (Fig. 6, G–I; and Table S1). Thus, the abundance of AZ components delivered to and incorporated at release sites can be differentially sculpted in number, size, intensity, and density yet ultimately tune the gain of global presynaptic output according to the total supply of AZ material with which a terminal is endowed.

PHP can be superimposed with AZ scaling and PHD to stabilize global synaptic strength

PHP is a well-studied form of homeostatic plasticity at the fly NMJ. Recent studies have demonstrated that AZs are rapidly

remodeled during PHP, where BRP, Unc13A, Cac, and other components increase in intensity and incorporate additional nanomodules following the rapid pharmacological or chronic genetic perturbation of postsynaptic glutamate receptors (Weyhersmüller et al., 2011; Goel et al., 2017; Li et al., 2018b; Böhme et al., 2019; Gratz et al., 2019). In addition, specific subsets of synapses within a single motor neuron can undergo homeostatic modulation during PHP (Newman et al., 2017; Li et al., 2018a), suggesting PHP signaling and expression operates with a high degree of compartmentalization and specificity at individual release sites. Importantly, PHD can be balanced with PHP over both acute and chronic timescales (Gaviño et al., 2015; Li et al., 2018b). We therefore sought to test whether three forms of homeostatic plasticity (PHP, PHD, and AZ scaling) can be functionally and structurally integrated at an individual NMJ.

We first asked if AZ scaling and PHP can be balanced to stabilize synaptic strength. We confirmed that 10-min application of the postsynaptic glutamate receptor antagonist philanthotoxin-433 (PhTx) to wild-type and vGlut-OE NMJs led to a decrease in mEPSP amplitude, as expected, but no significant change in EPSP amplitude because of a homeostatic increase in presynaptic release (Fig. 7, A–C; and Fig. S5, A–C). PhTx application to *rab3* mutants also induced robust PHP expression (Fig. S5, A–C), as previously shown (Müller et al., 2011), demonstrating that AZ scaling and PHP can be functionally balanced. Next, we tested whether AZ scaling, PHD, and PHP can be simultaneously induced and expressed at a single NMJ. As previously discussed, *endo* mutants exhibit both AZ scaling and PHD (Figs. 1, 2, and 3). To induce PHD in *rab3* mutants, we overexpressed *vGlut* in a *rab3* mutant background (*rab3*+vGlut-OE), which increased mEPSP amplitude but exhibited baseline levels of synaptic strength due a homeostatic reduction in quantal content (Fig. 7, A–C). Finally, we asked whether NMJs expressing AZ scaling and PHD could rapidly potentiate presynaptic release. Indeed, PhTx application to both *endo* and *rab3*+vGlut-OE induced robust PHP expression (Fig. 7, A–C). Thus, AZ scaling, PHD, and PHP can be fully integrated to maintain stable synaptic strength, revealing a high degree of balancing between independent and opposing homeostatic signaling systems.

PhTx application to wild-type NMJs induces a rapid enhancement in the levels of BRP and other AZ proteins. This rapid enhancement persists even when the axon is cut from the soma (Goel et al., 2017) and in the presence of translation inhibitors (Böhme et al., 2019), suggesting that active transport may rapidly mobilize a preexisting pool of additional AZ components to synapses. Because AZ and SV components are cotransported to presynaptic terminals via Arl8 (Fig. 6; Vukoja et al., 2018), we tested whether the SV protein vGlut, in addition to BRP, is enhanced at NMJs following PhTx application. Previous studies have assessed BRP intensity from separate populations of NMJs after fixation. However, we sought to image endogenous proteins from the same NMJ before and after 10-min incubation in PhTx; this would enable us to determine the proportion and properties of AZs that were modulated during PHP. To achieve this, we used endogenously tagged BRP-GFP and vGlut-GFP recently generated using a MiMIC transposon insertion library (Nagarkar-Jaiswal et al., 2015). We used live resonant scanning confocal imaging of BRP-GFP and vGlut-GFP in a semi-intact NMJ preparation at baseline and following 10-min incubation in PhTx (Fig. 7, D and E). We observed an increase in BRP-GFP at the same NMJ after PhTx application (Fig. 7, D and F–H) that was similar in magnitude to what we and others have found in fixed preparations (Weyhersmüller et al., 2011; Goel et al., 2017; Böhme et al., 2019; Gratz et al., 2019). Interestingly, we also observed a similar increase in vGlut intensity at both live and fixed NMJs following PhTx application (Fig. 7, E–J). Analysis of sum fluorescence intensity of individual BRP-GFP and vGlut-GFP puncta demonstrated that ∼84% of BRP puncta are significantly enhanced following PhTx application, with 16% showing no change or even a slight reduction in intensity (Fig. 7 F). A similar distribution was observed in the case of vGlut-GFP, where ∼70% of vGlut-GFP puncta were enhanced after PhTx application (Fig. 7 F). These findings parallel increases in endogenously tagged Cac at AZs before and following PhTx application (Gratz et al., 2019). Thus, live imaging of endogenous BRP and vGlut demonstrate enhanced levels of synaptic and AZ proteins occur during rapid PHP signaling.

Having established that *endo* and *rab3*+vGlut-OE NMJs can functionally express PHP in response to PhTx application, we finally tested whether BRP and vGlut levels are also enhanced at *endo* and *rab3*+vGlut-OE NMJs. In vGlut-OE and *rab3* NMJs alone, we find that BRP and vGlut levels are rapidly enhanced after PhTx application (Fig. S5, D–F). Interestingly, BRP levels are enhanced to similar degrees relative to the already increased baseline values in *rab3* mutants, revealing that the enlarged AZs in *rab3* mutants do not occlude the further remodeling observed following rapid PHP signaling. Next, we probed AZ structure following PhTx application to *endo* and *rab3*+vGlut-OE NMJs, which chronically express and functionally balance AZ scaling and PHD. AZs at both *endo* and *rab3*+vGlut-OE NMJs showed increased sum intensities of BRP and vGlut after PhTx application at individual AZs relative to their distinct baseline values (Fig. 7, I and J). Notably, the total fluorescence intensity of both BRP and vGlut over the entire NMJ was enhanced in each condition after PhTx application relative to their respective baseline values (Fig. 7 H). Thus, a preexisting pool of synaptic material is rapidly mobilized and incorporated into synapses during rapid PHP signaling, even at NMJs expressing PHD and AZ scaling.

Arl8-mediated transport of presynaptic cargo is necessary to remodel AZs and sustain the expression of PHP

The rapid increase in the total abundance of synaptic material present at NMJs following acute PHP signaling implies the existence of a "reserve pool" that can be harnessed to further modify synaptic structure during homeostatic plasticity. Given that AZ and SV components are cotransported to NMJs via Arl8, we next tested whether Arl8-mediated transport was necessary to mobilize synaptic cargo and enhance AZs during PHP signaling. We first imaged BRP and vGlut in wild type at baseline and following acute PhTx application to induce rapid PHP signaling. We also imaged these synaptic markers in *GluRIIA* mutants, in which genetic loss of postsynaptic glutamate receptors triggers the chronic expression of PHP over

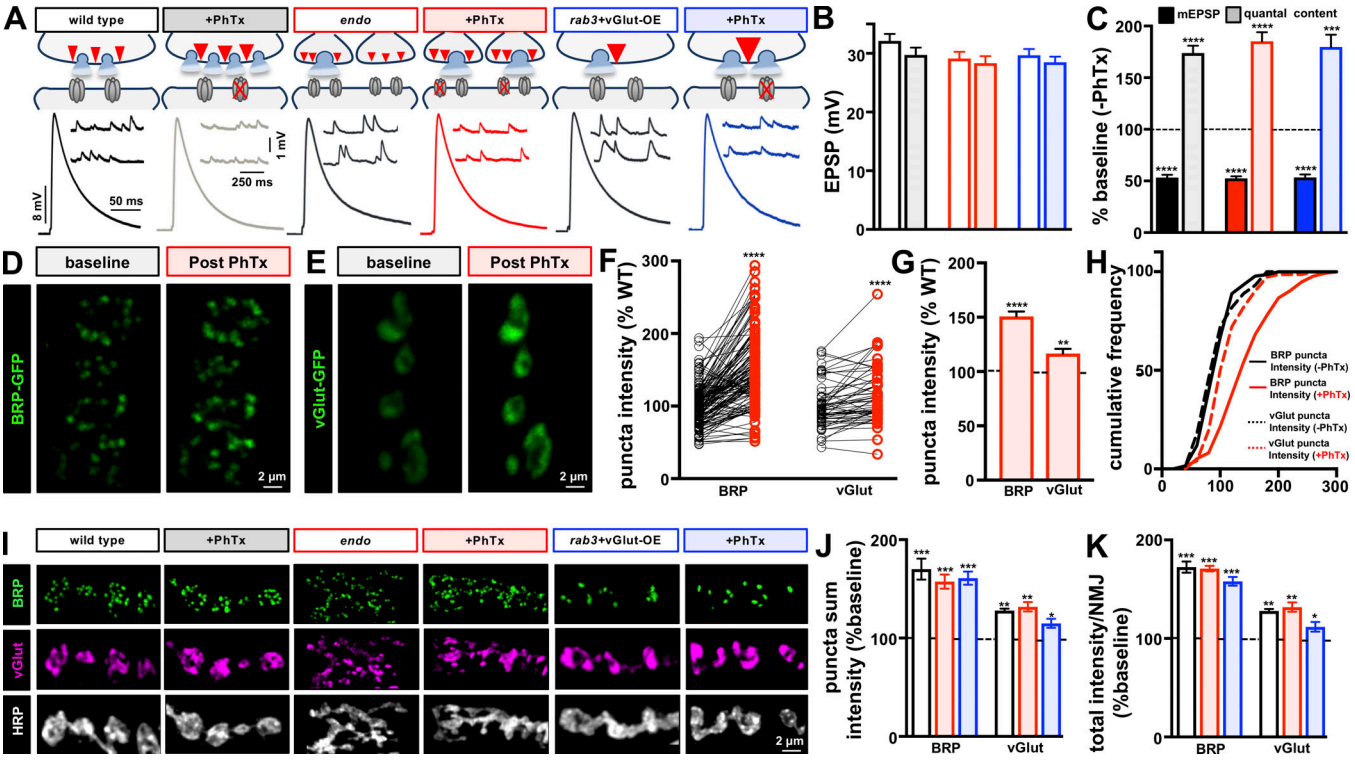

Figure 7. **Homeostatic potentiation can be balanced with both depression and AZ scaling. (A)** Schematic and representative traces of recordings from wild type, *endo*, and *rab3* mutants combined with *vGlut* overexpression (*rab3*+vGlut-OE: *w;OK6-Gal4,rab3^{rup}/rab3^{rup},UAS-vGlut*) before and after PhTx application. Diminished mEPSP amplitudes are observed following PhTx application, while EPSP amplitudes are maintained at baseline levels due to a homeostatic increase in presynaptic neurotransmitter release (quantal content). **(B and C)** Quantification of EPSP amplitude (B) and mEPSP and quantal content values (C) after PhTx application normalized as a percentage of baseline values (no PhTx treatment) in the indicated genotypes ($n \geq 6$; *t* test; Table S1). **(D and E)** Representative live images of muscle 6 NMJ boutons expressing endogenously tagged BRP-GFP (*w;BRP-GFP*; D) and vGlut-GFP (*w;vGlut-GFP*; E) at baseline and following 10-min incubation in PhTx. **(F–H)** Quantification of BRP and vGlut sum intensity of the same puncta before and following PhTx application (F), with an increased average (G) and rightward distribution (H) observed. $n \geq 135$, BRP; $n \geq 72$, vGlut; ratio paired *t* test (F), Student's *t* test (G), K-S test (H); Table S1. **(I)** Representative images of boutons immunostained with anti-BRP, anti-vGlut, and anti-HRP in the indicated genotypes before and following PhTx application. A parallel increase in BRP and vGlut intensity is observed in all genotypes following PhTx application. **(J)** Quantification of sum fluorescence intensity of BRP and vGlut puncta reveals a significant increase in each genotype following PhTx application compared with baseline (no PhTx). **(K)** Quantification of total fluorescence intensity of BRP and vGlut puncta per NMJ, showing an enhanced total abundance following PhTx application. Error bars indicate ± SEM ($n \geq 6$; *t* test; Table S1). *, $P < 0.05$; **, $P < 0.01$; ***, $P < 0.001$; ****, $P < 0.0001$; ns, not significant.

long timescales (Petersen et al., 1997). We observed that both BRP and vGlut were robustly increased at wild-type NMJs after PhTx and in *GluRIIA* mutants (Fig. 8, A–C), consistent with AZs being similarly remodeled after both acute and chronic expression of PHP (Weyhersmüller et al., 2011; Goel et al., 2017; Böhme et al., 2019; Gratz et al., 2019). To assess whether *arl8* was necessary for the delivery of this synaptic cargo during PHP signaling, we imaged BRP and vGlut in *arl8* mutants at baseline, after PhTx application, and in *GluRIIA; arl8* mutants. We found that BRP and vGlut failed to be enhanced over baseline values in *arl8*+PhTx and *GluRIIA;arl8* (Fig. 8, A–C). Thus, *arl8* is necessary to supply the synaptic cargo that is incorporated into AZs during the rapid induction and sustained expression of PHP.

Finally, we investigated whether the *arl8*-dependent enhancement in AZ structure was necessary for PHP expression. Distinct signaling systems control the rapid pharmacological induction versus the sustained expression of PHP over chronic timescales (Chen and Dickman, 2017; Goel et al., 2017; Böhme et al., 2019). One possibility is that the rapid remodeling of AZ structure is necessary to acutely express PHP, presumably by homeostatically potentiating release through enhanced AZ components. Alternatively, the rapid remodeling of AZ structure may be dispensable for acute PHP expression but necessary to sustain PHP expression over longer timescales. In this scenario, the rapid enhancement of AZ structure may "seed" the adaptations necessary to sustain PHP expression in anticipation of chronic potentiation, but other processes operate to enable rapid PHP expression independently of AZ addition. We observed that PhTx application to *arl8* mutants reduced mEPSP amplitudes and initiated a robust increase in quantal content that restored EPSP values to baseline levels (Fig. 8, D–F). However, PHP failed to be sustained over chronic timescales in *GluRIIA;arl8* double mutants (Fig. 8, D–F). Therefore, the rapid remodeling of AZ structure appears to be surprisingly dispensable for PHP expression over short timescales but is absolutely necessary to sustain PHP expression over longer temporal periods.

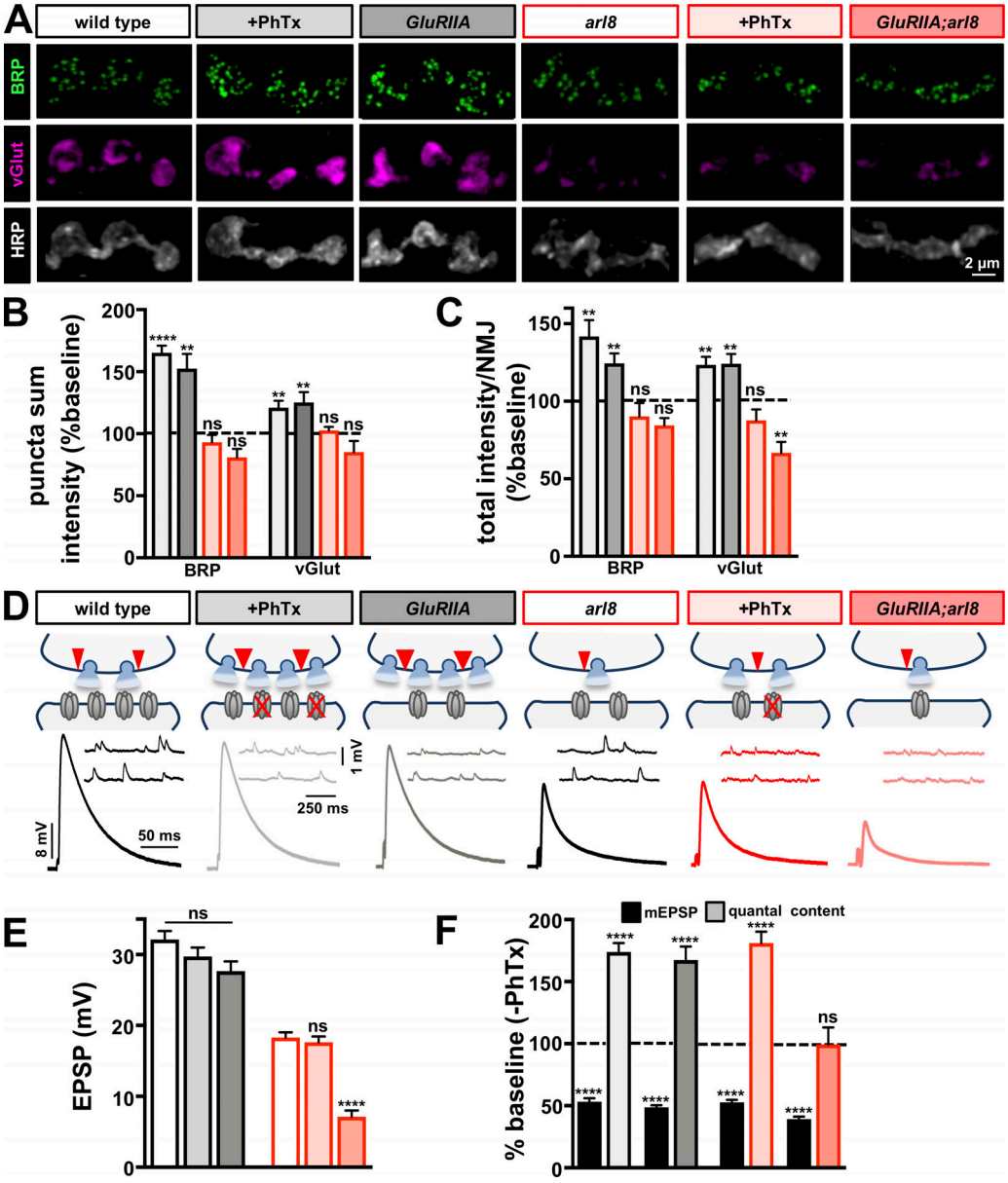

Figure 8. ***arl8* is necessary for the rapid remodeling of AZ structure during homeostatic signaling and for the chronic expression of PHP.** **(A)** Representative images of NMJs immunostained with anti-BRP, anti-vGlut, and anti-HRP of wild type and *arl8* mutants at baseline and following PhTx application, as well as *GluRIIA* mutants (*w;GluRIIA*^{sp16}) and *GluRIIA;arl8* double mutants (*w;GluRIIA*^{sp16}*;arl8*^{e00336}). **(B)** Quantification of BRP and vGlut puncta sum intensity in the indicated conditions normalized to baseline values (no PhTx application for wild type and *arl8* mutants, wild type for *GluRIIA* mutants, *arl8* for *GluRIIA;arl8* mutants). Note that while both BRP and vGlut intensity is enhanced following PhTx application to wild type and in *GluRIIA* mutants, no change in intensity is observed in *arl8*+PhTx nor in *GluRIIA;arl8* mutants compared with their baseline values. **(C)** Quantification of total sum intensity of BRP and vGlut per NMJ demonstrates a failure to increase AZ and SV components at presynaptic terminals in *arl8*+PhTx and *GluRIIA;arl8* double mutants. **(D)** Schematic and representative traces of recordings from the indicated genotypes and conditions. Note that while mEPSP amplitudes are reduced following PhTx application or by loss of *GluRIIA*, as expected, rapid PHP is robustly expressed following acute application of PhTx. However, PHP fails to be expressed over chronic timescales in *GluRIIA;arl8* double mutants. **(E)** Quantification of EPSP amplitude in the indicated genotypes. **(F)** mEPSP and quantal content values in the indicated genotypes normalized to baseline values demonstrating that while PHP can be rapidly induced by PhTx application to wild-type and *arl8* NMJs, PHP fails to be chronically expressed in *GluRIIA;arl8*. Error bars indicate ± SEM ($n \geq 7$; *t* test; Table S1). **, P < 0.01; ****, P < 0.0001; ns, not significant.

Discussion

We have investigated how global synaptic strength is maintained at NMJs when the total number of AZs is enhanced or reduced. Our analysis reveals that the level of scaffolds at individual AZs is inversely modulated with number across an entire NMJ, while the total abundance of AZ material remains constant. Superresolution microscopy reveals modular AZ nanoarchitecture that can be expanded or contracted while maintaining consistent stoichiometric ratios between AZ components. Axonal transport of presynaptic cargo via Arl8 can tune the abundance of AZ components to modulate the gain of neurotransmitter release and is also necessary to mobilize additional

synaptic cargo to NMJs during homeostatic signaling to sustain enhanced neurotransmission. Together, our data demonstrate that AZs are elastic nodes of modulation, capable of adaptive remodeling in response to synaptic overgrowth, AZ density, or diminished postsynaptic receptor functionality to calibrate presynaptic efficacy and ensure stable global levels of synaptic strength.

Homeostatic tuning of AZ size

There is considerable heterogeneity in the intensity, size, and architecture of individual AZs, both between and within neuronal subtypes (Guerrero et al., 2005; Ehmann et al., 2014; Van Vactor and Sigrist, 2017; Akbergenova et al., 2018; Gratz et al., 2019). What functional impact does this variation have on release probability? Several recent studies have established that the size, intensity, and/or abundance of material at individual AZs positively correlates with both calcium influx and release probability at the fly NMJ (Marrus and DiAntonio, 2004; Kittel et al., 2006; Graf et al., 2009; Peled and Isacoff, 2011; Melom et al., 2013; Akbergenova et al., 2018; Gratz et al., 2019). BRP controls the size of the readily releasable SV pool (Matkovic et al., 2013), Unc13A defines SV release sites (Böhme et al., 2016; Reddy-Alla et al., 2017), and Ca^{2+} channel abundance at specific AZs is a major determinant of Ca^{2+} levels (Akbergenova et al., 2018; Gratz et al., 2019). Indeed, functional imaging has demonstrated that BRP and Ca^{2+} channel intensity scales with release probability at individual AZs and that these properties are major molecular determinants of the heterogeneity of release probability (Melom et al., 2013; Paul et al., 2015; Akbergenova et al., 2018; Gratz et al., 2019). Parallel changes in AZ dimensions have been observed to tune presynaptic efficacy in mammals (Murthy et al., 2001; Matz et al., 2010; Holderith et al., 2012; Glebov et al., 2017; Lübbert et al., 2019). In both *endo* and *rab3* mutants, a change in the total number of AZs per NMJ should lead to an decrease or increase in synaptic strength if release probability remained the same for each AZ. However, as the levels of AZ scaffolding scale inversely with number, global neurotransmitter release is maintained at levels unchanged from wild type. Importantly, nanomodular units of AZ "quanta" have been noted here and by others in *Drosophila* (Böhme et al., 2019), and quantal elasticity of synaptic nanostructure at mammalian synapses has been described (Tang et al., 2016; Biederer et al., 2017; Hruska et al., 2018). In *endo* and *rab3* mutant NMJs, these modules are scaled and redistributed across all AZs while maintaining the same total intensity as wild-type NMJs. Notably, postsynaptic structures mirror this presynaptic architecture. This is highlighted by the remarkable symmetry observed on both sides of the synapse in *endo* mutants (Fig. S5; Dickman et al., 2006) and even in the pairing of enlarged AZs opposite enhanced glutamate receptor fields in *rab3* mutants (Marrus and DiAntonio, 2004). Indeed, an intercellular dialog between pre- and postsynaptic structures is likely to coordinate the formation and stabilization of the synaptic dyad (Biederer et al., 2017). Such modularity of AZ nanostructure provides a simple and elegant mechanism that enables scaling of AZ size and number across an entire terminal to tune local and yet preserve global presynaptic release probability.

Given that multiple forms of synaptic plasticity can operate with specificity at individual pre- and postsynaptic compartments, how is global neurotransmitter output established and maintained across the terminals of a single neuron? One attractive possibility is that the abundance of AZ material, heterogeneously distributed at neuronal terminals, sets global synaptic strength. In this model, a limited abundance of synaptic cargo provides the "clay" to be sculpted with varying size, number, and density of release sites while maintaining stable global presynaptic release probability. Clearly, a substantial reserve pool of AZ components exists that does not require new protein synthesis (Böhme et al., 2019), implying that the supply of AZ material itself is not rate limiting and that additional layers of regulation ultimately determine the levels of AZs components incorporated into functional release sites during development and plasticity. There is intriguing recent evidence from mammalian central synapses that a gradient of decreasing AZ size from the soma serves to modulate release properties to tune input frequencies at specific dendritic domains (Grillo et al., 2018). Thus, multiple signaling systems have the capacity to adjust AZ structure and calibrate release probability with both local and global layers of control.

AZs as substrates to sustain the homeostatic modulation of global synaptic strength

Although PHD and PHP are independent forms of plasticity (Gaviño et al., 2015; Li et al., 2018b), it is clear that these processes can be balanced together with the scaling of AZs in *endo* and *rab3* mutants to maintain stable synaptic strength. PHD is a homeostat triggered by excess glutamate release (Daniels et al., 2004; Gaviño et al., 2015; Li et al., 2018b). However, in contrast to PHP and AZ scaling, PHD does not appear to involve any obvious adaptations in AZ number or structure and rather operates to reduce global presynaptic release probability exclusively through functional changes (Li et al., 2018b; Gratz et al., 2019), likely via reduced presynaptic calcium influx (Gaviño et al., 2015). In contrast, AZ structures are remodeled during PHP signaling in response to acute or chronic perturbations to postsynaptic glutamate receptors (Weyhersmüller et al., 2011; Goel et al., 2017; Li et al., 2018b; Böhme et al., 2019; Gratz et al., 2019). Importantly, PHP and PHD are forms of plasticity that serve as stress responses to perturbations that disrupt synaptic function or glutamate levels outside of stable physiological ranges. In contrast, AZ scaling is likely to be intimately coupled to and integrated with the ongoing processes of synaptic development, growth, and neurotransmission.

PHP has the capacity to modulate the strength of individual presynaptic compartments with a high degree of precision and specificity (Kiragasi et al., 2017; Newman et al., 2017; Li et al., 2018a). Indeed, there is evidence that a reduced state of glutamate receptor functionality opposing specific release sites determines PHP expression at these AZs, while neighboring synapses within the same motor neuron opposed by unperturbed receptors do not change (Li et al., 2018a). Thus, if hundreds of individual synapses operate as independent homeostats for the transsynaptic, retrograde control of PHP, then how does this signaling system interface with the target-specific, global

control of synaptic strength? One possibility is that set point levels of global synaptic strength may be established by factors that control the expression and delivery of key synaptic components. For example, Arl8-mediated transport of presynaptic cargo couples the delivery of SV and AZ components and modulates the gain of baseline neurotransmission and is also necessary to mobilize additional synaptic material to sustain PHP expression (Figs. 6 and 8; Vukoja et al., 2018). It seems likely that other factors are also involved in regulating the transport of presynaptic cargo during chronic homeostatic potentiation to sustain the robust tuning of release probability (Böhme et al., 2019).

It is surprising that the remodeling of AZ structure observed following acute perturbation of postsynaptic receptors is not required for the rapid expression of PHP. Live imaging of BRP and vGlut (Fig. 7), as well as Cac (Gratz et al., 2019), before and following PhTx application revealed rapid mobilization of synaptic material to release sites during PHP signaling. The robust expression of this process, even when protein synthesis is blocked and the axon is severed from the cell body (Goel et al., 2017; Böhme et al., 2019), implies a preexisting but seemingly invisible "reserve pool" of synaptic material can be mobilized. Although the origin of this pool is unclear, Arl8 and other motor transport systems are required to transport and incorporate these components into AZs (Böhme et al., 2019), suggesting that mobilization of diffuse cargos from axons and cytosolic pools may be involved. In principle, the accumulation of additional AZ scaffolds and Ca^{2+} channels provide a robust and attractive mechanism to explain the increased release probability characteristic of PHP by accounting for two key expression mechanisms: (1) enhancements in presynaptic Ca^{2+} influx (Müller and Davis, 2012) due to increased Cac abundance, which predicts Ca^{2+} influx and release probability at individual AZs (Akbergenova et al., 2018; Gratz et al., 2019); and (2) increased size of the readily releasable vesicle pool (Weyhersmüller et al., 2011) due to increased BRP abundance, which controls the size of this pool (Matkovic et al., 2013). However, we find that AZ remodeling is blocked in *arl8* mutants but that rapid PHP is robustly expressed (Fig. 8). A recent study also found that AZ remodeling is blocked in *brp* mutants but that rapid PHP is expressed (Böhme et al., 2019). This implies other mechanisms, such as phosphorylation or ubiquitination, are necessary to express rapid PHP (Hauswirth et al., 2018; Kikuma et al., 2018 *Preprint*; Wentzel et al., 2018). Over chronic timescales, however, the sustained expression of PHP requires both *arl8* and *brp* (Fig. 8; Böhme et al., 2019), indicating that AZ remodeling is ultimately necessary to sustain homeostatic potentiation. It is interesting to note that AZ size and density can be dynamically reorganized in hours in *rab3* mutants (Graf et al., 2009), and it is tempting to speculate that a similar time course requires AZ remodeling to sustain chronic PHP expression.

In contrast to synapse-specific compartmentalization of PHP signaling, global control of synaptic strength should be responsive to the needs of the entire target, which is the muscle being innervated by the motor neuron in the case of the NMJ. Therefore, AZ scaling should be controlled not with specificity for individual release sites but rather toward the entire target being innervated. Indeed, there is intriguing evidence that a homeostat governs global synaptic strength at the NMJ with target specificity. When one muscle is forced to be hyperinnervated and an adjacent muscle hypoinnervated by the same motor neurons at the *Drosophila* NMJ, two distinct forms of homeostatic plasticity were initiated that stabilized global synaptic strength at each muscle (Davis and Goodman, 1998). A homeostatic reduction in presynaptic release probability was induced in the hyperinnervated NMJ (Davis and Goodman, 1998), akin to what we observed for *endo* mutants, although the expression mechanism for this form of plasticity has not yet been defined. In contrast, the hypoinnervated NMJ does not appear to adjust presynaptic release; rather, an increase in quantal size was observed (Davis and Goodman, 1998) due to a homeostatic increase in postsynaptic glutamate receptor abundance (Goel and Dickman, 2018). Parallel observations have been made at mammalian central synapses, where heterogeneity in release probability was found along terminals innervating a specific dendritic branch (Matsuzaki et al., 2004; Branco et al., 2008), which may also use adaptive changes in AZ size and structure (Murthy et al., 2001; Grillo et al., 2018). While both Hebbian and homeostatic plasticity mechanisms can operate locally with specificity at individual synapses (Turrigiano, 2012), global homeostatic mechanisms are sensitive to the state of an entire target and scale synaptic strength across individual sites.

Synapses must maintain the flexibility required for learning and memory throughout life while still ensuring the stability necessary to protect coherent information transfer. These competing demands imply the existence of robust homeostatic forces that operate on both sides of the synapse to dynamically adjust presynaptic release and postsynaptic responsiveness. There is evidence that the abundance of postsynaptic glutamate receptors can homeostatically scale across the dendrites of individual neurons in response to changes in presynaptic activity (Turrigiano et al., 1998; Hou et al., 2011). We have presented evidence for a mirrored process across the presynaptic terminals of individual neurons, where the abundance of AZ material is adaptively scaled to maintain stable synaptic strength. These pre- and postsynaptic processes could work independently or in conjunction to adapt to altered innervation (Davis and Goodman, 1998; Branco et al., 2008; Tokuoka and Goda, 2008), excitability (Murthy et al., 2001; Paradis et al., 2001), activity (Butz et al., 2009; Holtmaat and Svoboda, 2009), injury (Goel and Dickman, 2018), and even sleep (Bushey et al., 2011; Hengen et al., 2016; Diering et al., 2017; Kikuma et al., 2018 *Preprint*). The complex interplay of Hebbian and homeostatic regulation operating locally and globally, over distinct spatiotemporal scales and at both pre- and postsynaptic compartments, endows synapses with this astonishing combination of flexibility and stability.

Materials and methods

Fly stocks

Drosophila stocks were raised at 25°C on standard molasses food. The w^{1118} strain was used as the wild-type control unless otherwise noted, as this is the genetic background of the transgenic lines and other genotypes used in this study. The following fly

stocks were used: *endo*^{1} and *endo*$^{\Delta 4}$ (Verstreken et al., 2002), *GluRIIA*^{sp16} (Petersen et al., 1997), *OK371-Gal4* (Mahr and Aberle, 2006), *OK6-Gal4* (Aberle et al., 2002), *UAS-vGlut* (Daniels et al., 2004), *rab3*^{rup} (Graf et al., 2009), *Cac*$^{sfGFP\text{-}N}$ (Gratz et al., 2019), and *UAS-arl8-GFP* and *arl8*^{e00336} (Vukoja et al., 2018). All other *Drosophila* stocks were obtained from the Bloomington Drosophila Stock Center (BDSC): *elav*^{c155}*-Gal4* (BDSC #458), *endo* RNAi (BDSC #27679), *rab3* RNAi (BDSC #31691), BRP-GFP (BDSC #59292), and vGlut-GFP (BDSC #59411). Details of all stocks and their source are listed in Table S2.

Immunocytochemistry

Third-instar larvae were dissected in ice-cold 0 Ca^{2+} HL-3 and fixed in Bouin's fixative for 5 min, 100% ice-cold methanol for 5 min, or 4% PFA for 10 min as described previously (Böhme et al., 2016; Perry et al., 2017). Briefly, larvae were washed with PBS containing 0.1% Triton X-100 (PBST) for 30 min, blocked with 5% normal donkey serum followed by overnight incubation in primary antibodies at 4°C, three washes in PBST, incubation in secondary antibodies for 2 h, three final washes in PBST, and equilibration in 70% glycerol in PBST. Samples were mounted in VectaShield (Vector Laboratories) or ProLong Gold Antifade Reagent (Cell Signaling Technology) for Confocal and STED imaging, respectively. The following antibodies were used: mouse anti-BRP (nc82; 1:100; Developmental Studies Hybridoma Bank [DSHB]), mouse anti-Synapsin, (3C11; 1:10; DSHB), rabbit anti-SYT1 (1:2,500; Mackler et al., 2002), guinea pig anti-vGlut (1:1,000; Chen et al., 2017), guinea pig anti-Unc13A (1:500; Böhme et al., 2016), and affinity-purified rabbit anti-GluRIII (1:2,000; Marrus and DiAntonio, 2004). For confocal imaging, donkey anti-mouse, anti-guinea pig, and anti-rabbit Alexa Fluor 488–, Cyanine 3–, and Alexa Fluor 647–conjugated goat anti-HRP and DyLight 405–conjugated secondary antibodies were used at 1:400 (Jackson ImmunoResearch). For STED imaging, BRP and Unc13A primary antibodies were used and goat anti-guinea pig star635 (1:100; 1–0101002; Abberior) and goat anti-mouse Alexa Fluor 594 (1:500; A11032; Thermo Fisher Scientific) were used for secondary antibodies. Details of all antibodies used, including their source and catalog numbers, are listed in Table S2.

Confocal imaging and analysis

Samples were imaged double blind with respect to researcher and genotype using a Nikon A1R Resonant Scanning Confocal microscope equipped with NIS Elements software and a 100× APO 1.4-NA oil-immersion objective using separate channels with four laser lines (405, 488, 561, and 637 nm) at room temperature. Boutons were counted using vGlut and HRP-stained NMJ terminals on muscle 6/7 and muscle 4 of segment A3, considering each vGlut puncta to be a bouton. For fluorescence quantifications of SV markers and AZ proteins, all genotypes within a dataset were immunostained in the same tube with identical reagents and then mounted and imaged in the same session. Z-stacks were obtained using identical settings for all genotypes with z axis spacing between 0.15 and 0.2 µm within an experiment and optimized for detection without saturation of the signal. Maximum intensity projections were used for quantitative image analysis with the NIS Elements software General Analysis toolkit. Synapse surface area was calculated by creating a mask around the HRP channel that labels the neuronal membrane.

To quantify mean puncta intensity, fluorescence intensity thresholds and filters were applied to the relevant channel, and the mean puncta intensity was calculated as the total fluorescence intensity signal of the puncta divided by the area of the puncta. To quantify sum puncta intensity, the total fluorescence intensity signal of the individual puncta was calculated without regard to area. For each particular sample set, thresholds were optimized to capture the dynamic range of intensity levels in the wild-type sample. This threshold was then used to image all other genotypes in the same sample set, and all intensities were normalized to wild-type values within an experimental set. AZs too closely spaced to be resolved (~2.5% of all analyzed) were excluded from the analysis. Finally, to quantify total intensity per NMJ, the sum fluorescence intensity for each individual puncta was summed across the entire NMJ for all puncta. For immunostaining experiments following PhTx application, preparations were treated as described for electrophysiological experiments, fixed with 100% ethanol for 5 min, and stained as above. Similar enhancements in BRP puncta intensity after PhTx application were observed after fixation using Bouin's fixative, 4% PFA, or 100% methanol (Table S1).

To validate the quantification for BRP, Unc13A, or Cac puncta area in wild type, *endo*, and *rab3*, we performed full width at half maximum analysis for images of individual puncta using NIS Elements software. This measurement determines the apparent width of the individual puncta where intensity is 50% of the maximum value. The value given by full width at half maximum thus provides an internal validation of relative puncta size. While this apparent puncta area may not precisely match the values obtained through other approaches (e.g., STED and EM), relative changes are internally consistent.

Live imaging and analysis

Live imaging of BRP-GFP and vGlut-GFP before and after PhTx application was performed on a Nikon A1R Resonant Scanning Confocal microscope equipped with NIS Elements software and a 60× APO 1.0-NA water-immersion objective using the 488 laser line at room temperature. Third-instar larvae were minimally dissected in Ca^{2+}-free HL3, with one side of the body wall gently pinned to avoid stretching. Before PhTx treatment, Z-stacks of NMJ 6/7 were acquired using the resonant scanner with 6× scan zoom. Preparations were then exposed to 40 µM PhTx. Because segmental nerves were left intact, experiments were performed in Ca^{2+}-free HL3 to minimize muscle contractions and movement during imaging, a condition that does not impact PHP signaling (Goel et al., 2017). Immediately following 10-min PhTx treatment, NMJs were reimaged using the same parameters. To measure intensity at individual BRP and vGlut puncta, Z-stacks were flattened using the maximum intensity Z-projection function and background subtracted using the same threshold values before and after PhTx treatment. A local contrast function was used to aid in BRP puncta recognition and masking. For each BRP or vGlut puncta, a region of interest was created and analyzed before and after PhTx treatment, and

the sum intensity of the region of interest was then quantified. Data are reported from three different NMJs for BRP-GFP and vGlut-GFP. For consistency, analysis was restricted to type Ib boutons of NMJ 6/7.

STED imaging and analysis

STED microscopy was performed using a Leica Microsystems TCS SP8 gSTED 3× setup equipped with a pulsed white-light laser (~80-ps pulse width, 80-MHz repetition rate; NKT Photonics) and two STED lasers for depletion (continuous wave at 592 nm, pulsed at 775 nm). The pulsed 775-nm STED laser was triggered by the white-light laser. Images were acquired with a 100×, 1.4-NA oil-immersion objective at room temperature. 512 × 512-pixel resolution 2D STED images were scanned at 400 Hz using 4× line averaging and frame accumulation 4×. The lateral pixel size was set to values of ~13 nm. All images within one dataset were acquired with the same microscope settings. 12 images over 4 larval filets were acquired per genotype. Images were processed using the Huygens deconvolution software (Scientific Volume Imaging) using a theoretical point spread function automatically computed based on a pulsed STED-optimized function and the specific microscope parameters. Default deconvolution settings were applied. Contrast and brightness were adapted for visualization only, where necessary, using ImageJ software.

The numbers of BRP and Unc13A modules were analyzed using ImageJ software as described previously (Böhme et al., 2019). In-focus planar AZs were manually chosen, and modules were counted automatically using the Find Maxima function with a noise tolerance of 0 to detect the position of cluster centers (local intensity maxima). To prevent detection of the same cluster more than once, a defined minimum distance of 50 nm was used and only the local maximas with the highest intensity values were considered. Maximas found outside the AZ, as defined by the BRP and Unc13A ring, were ignored. This resulted in a categorization of AZs of wild type, endo^{RNAi}, and *rab3* in different classes, with the most frequent number of clusters per AZ being the representative modular number for that genotype. The histogram and cumulative frequency plot shown in Fig. 5 (I and J) were generated by counting the number of images in each cluster number class and dividing each value by the total amount of AZs in all classes for different genotypes.

Electrophysiology

All dissections and recordings were performed in modified HL-3 saline (Stewart et al., 1994; Kikuma et al., 2017) containing (in mM): 70 NaCl, 5 KCl, 10 $MgCl_2$, 10 $NaHCO_3$, 115 sucrose, 5 trehelose, 5 Hepes, and 0.4 $CaCl_2$ (unless otherwise specified), pH 7.2. NMJ sharp electrode (electrode resistance between 10–35 MΩ) recordings were performed on muscles 6 or 4 of abdominal segments A2 and A3 in wandering third-instar larvae (Goel et al., 2019b). Relative data from muscles 6 or 4 were similar; recordings from muscle 6 are presented in the figures, while the data from muscle 4 are shown in Table S1. Recordings were performed on an Olympus BX61 WI microscope using a 40×/0.80 water-dipping objective. Recordings were acquired using an Axoclamp 900A amplifier, Digidata 1440A acquisition system, and pClamp 10.5 software (Molecular Devices). Electrophysiological sweeps were digitized at 10 kHz and filtered at 1 kHz. Data were analyzed using Clampfit (Molecular devices), MiniAnalysis (Synaptosoft), and Excel (Microsoft) software.

mEPSPs were recorded in the absence of any stimulation and cut motor axons were stimulated to elicit EPSPs. An ISO-Flex stimulus isolator (A.M.P.I.) was used to modulate the amplitude of stimulatory currents. Intensity was adjusted for each cell, set to consistently elicit responses from both neurons innervating the muscle segment, but avoiding overstimulation. Average mEPSP, EPSP, and quantal content were calculated for each genotype. Muscle input resistance (R_{in}) and resting membrane potential (V_{rest}) were monitored during each experiment. Recordings were rejected if the V_{rest} was more depolarized than −60 mV, if the R_{in} was less than 5 MΩ, or if either measurement deviated by more than 10% during the course of the experiment. Larvae were incubated with or without PhTx (20 µM; Sigma) resuspended in HL-3 for 10 min, as described previously (Frank et al., 2006; Dickman and Davis, 2009).

EM

EM analysis was performed as described previously (Atwood et al., 1993). Wandering third-instar larvae were dissected in Ca^{2+}-free HL-3 and then fixed in 2.5% glutaraldehyde/0.1 M cacodylate buffer at 4°C. Larvae were then washed three times for 20 min in 0.1 M cacodylate buffer. The larval pelts were then placed in 1% osmium tetroxide/0.1M cacodylate buffer for 1 h at room temperature. After washing the larva twice with cacodylate and twice with water, larvae were then dehydrated in ethanol. Samples were cleared in propylene oxide and infiltrated with 50% Eponate 12 in propylene oxide overnight. The following day, samples were embedded in fresh Eponate 12. EM sections were obtained on a Morgagni 268 transmission electron microscope (FEI). NMJs were serial sectioned at a 60- to 70-nm thickness. The sections were mounted on Formvar-coated single slot grids and viewed at a 23,000 magnification and were recorded with a Megaview II CCD camera. Images were analyzed blind to genotype using the general analysis toolkit in the NIS Elements software and ImageJ software.

Statistical analysis

Data were analyzed using GraphPad Prism (version 7.0) or Microsoft Excel software (version 16.22). Sample values were tested for normality using the D'Agostino and Pearson omnibus normality test, which determined that the assumption of normality of the sample distribution was not violated. Data were then compared using either a one-way ANOVA and tested for significance using a Tukey's multiple comparison test or an unpaired two-tailed *t* test with Welch's correction. Cumulative frequency distributions were tested for significance using the Kolmogorov–Smirnov (K-S) test. For individual puncta intensity analysis before and after PhTx (Fig. 7 F), a ratio paired *t* test was used. For STED imaging, the cumulative frequency plots were made smooth using

GraphPad Prism Smoothing algorithm default settings (four neighbors averaged on each size and a second-order smoothing polynomial). All data are presented as mean ± SEM; *n* indicates sample number, and P denotes the level of significance assessed (*, P < 0.05; **, P < 0.01; ***, P < 0.001; ****, P < 0.0001; ns, not significant). Statistics of all experiments are summarized in Table S1.

Online supplemental material

Fig. S1 demonstrates distinct mechanisms enlarge quantal size in *endo* and vGlut-OE. Fig. S2 shows that SV recycling is unperturbed in vGlut-OE. Fig. S3 displays a mirroring of postsynaptic glutamate receptor fields with presynaptic AZ structure. Fig. S4 shows ultrastructural analysis of T-bar width and AZ length in *endo*. Fig. S5 demonstrates that homeostatic depression and AZ scaling can be balanced with rapid homeostatic potentiation. Table S1 summarizes all the statistics related to imaging (confocal, STED, and EM) and electrophysiology. Table S2 details the antibodies and *Drosophila* stocks used in this study.

Acknowledgments

We thank Aaron DiAntonio (Washington University, St. Louis, MO) and Volker Hauke (Leibniz-Forschungsinstitut für Molekulare Pharmakologie, Berlin, Germany) for sharing *Drosophila* stocks and Noreen Reist (Colorado State University, Fort Collins, CO) for generously sharing the anti-Synaptotagmin antibody. We particularly thank Kate O'Connor-Giles (Brown University, Providence, RI) for sharing the $cac^{sfGFP\text{-}N}$ stock before publication. We acknowledge the DSHB (Iowa) for antibodies used in this study, and the BDSC for fly stocks (National Institutes of Health grant P40OD018537). We thank Yu-Chen Huang, Patrick Keenan, Andrew Brumm, and Ramunas Stanciauskas (Nikon Instruments) for technical advice and optimization of the software for imaging acquisition and analysis.

P. Goel was supported in part by a University of Southern California Provost Graduate Research Fellowship. This work was supported by the Deutsche Forschungsgemeinschaft (Emmy Noether Program [A.M. Walter] and grant SFB958 [S.J. Sigrist]), the National Institutes of Health (grant NS091546), and the Mallinckrodt and Klingenstein-Simons Foundation (research fellowships to D. Dickman).

The authors declare no competing financial interests.

Author contributions: P. Goel contributed all experiments except STED imaging and analysis. L. Nunnelly helped rear and dissect *endo* larvae during early stages of the project. D.D. Bergeron contributed STED imaging and analysis, with input from M.A. Böhme, A.M. Walter, and S.J. Sigrist. C. Buser contributed EM preparation and image acquisition, and M. Lehmann contributed use of the STED microscope and analysis. P. Goel and D. Dickman wrote the manuscript, with comments from A.M. Walter and S.J. Sigrist.

Submitted: 23 July 2018
Revised: 14 December 2018
Accepted: 6 March 2019

References

Aberle, H., A.P. Haghighi, R.D. Fetter, B.D. McCabe, T.R. Magalhães, and C.S. Goodman. 2002. wishful thinking encodes a BMP type II receptor that regulates synaptic growth in Drosophila. *Neuron.* 33:545–558. https://doi.org/10.1016/S0896-6273(02)00589-5

Akbergenova, Y., K.L. Cunningham, Y.V. Zhang, S. Weiss, and J.T. Littleton. 2018. Characterization of developmental and molecular factors underlying release heterogeneity at *Drosophila* synapses. *eLife.* 7:e38268. https://doi.org/10.7554/eLife.38268

Atwood, H.L., C.K. Govind, and C.F. Wu. 1993. Differential ultrastructure of synaptic terminals on ventral longitudinal abdominal muscles in Drosophila larvae. *J. Neurobiol.* 24:1008–1024. https://doi.org/10.1002/neu.480240803

Biederer, T., P.S. Kaeser, and T.A. Blanpied. 2017. Transcellular Nanoalignment of Synaptic Function. *Neuron.* 96:680–696. https://doi.org/10.1016/j.neuron.2017.10.006

Böhme, M.A., C. Beis, S. Reddy-Alla, E. Reynolds, M.M. Mampell, A.T. Grasskamp, J. Lützkendorf, D.D. Bergeron, J.H. Driller, H. Babikir, et al. 2016. Active zone scaffolds differentially accumulate Unc13 isoforms to tune Ca(2+) channel-vesicle coupling. *Nat. Neurosci.* 19:1311–1320. https://doi.org/10.1038/nn.4364

Böhme, M.A., A.W. McCarthy, A.T. Grasskamp, C.B. Beuschel, P. Goel, B. Jusyte, D. Laber, S. Huang, U. Rey, A.G. Petzold, et al. 2019. Rapid active zone remodeling consolidates presynaptic potentiation. *Nat. Commun.* 10:1085. https://doi.org/10.1038/s41467-019-08977-6

Branco, T., K. Staras, K.J. Darcy, and Y. Goda. 2008. Local dendritic activity sets release probability at hippocampal synapses. *Neuron.* 59:475–485. https://doi.org/10.1016/j.neuron.2008.07.006

Broadie, K., and M. Bate. 1995. The Drosophila NMJ: a genetic model system for synapse formation and function. *Semin. Dev. Biol.* 6:221–231. https://doi.org/10.1016/S1044-5781(06)80031-9

Budnik, V., Y.H. Koh, B. Guan, B. Hartmann, C. Hough, D. Woods, and M. Gorczyca. 1996. Regulation of synapse structure and function by the Drosophila tumor suppressor gene *dlg*. *Neuron.* 17:627–640. https://doi.org/10.1016/S0896-6273(00)80196-8

Bushey, D., G. Tononi, and C. Cirelli. 2011. Sleep and synaptic homeostasis: structural evidence in Drosophila. *Science.* 332:1576–1581. https://doi.org/10.1126/science.1202839

Butz, M., F. Wörgötter, and A. van Ooyen. 2009. Activity-dependent structural plasticity. *Brain Res. Brain Res. Rev.* 60:287–305. https://doi.org/10.1016/j.brainresrev.2008.12.023

Chen, X., and D. Dickman. 2017. Development of a tissue-specific ribosome profiling approach in Drosophila enables genome-wide evaluation of translational adaptations. *PLoS Genet.* 13:e1007117. https://doi.org/10.1371/journal.pgen.1007117

Chen, C.K., C. Bregere, J. Paluch, J.F. Lu, D.K. Dickman, and K.T. Chang. 2014. Activity-dependent facilitation of Synaptojanin and synaptic vesicle recycling by the Minibrain kinase. *Nat. Commun.* 5:4246. https://doi.org/10.1038/ncomms5246

Chen, X., W. Ma, S. Zhang, J. Paluch, W. Guo, and D.K. Dickman. 2017. The BLOC-1 Subunit Pallidin Facilitates Activity-Dependent Synaptic Vesicle Recycling. *eNeuro.* 4:1–18. https://doi.org/10.1523/ENEURO.0335-16.2017

Daniels, R.W., C.A. Collins, M.V. Gelfand, J. Dant, E.S. Brooks, D.E. Krantz, and A. DiAntonio. 2004. Increased expression of the Drosophila vesicular glutamate transporter leads to excess glutamate release and a compensatory decrease in quantal content. *J. Neurosci.* 24:10466–10474. https://doi.org/10.1523/JNEUROSCI.3001-04.2004

Davis, G.W. 2013. Homeostatic signaling and the stabilization of neural function. *Neuron.* 80:718–728. https://doi.org/10.1016/j.neuron.2013.09.044

Davis, G.W., and C.S. Goodman. 1998. Synapse-specific control of synaptic efficacy at the terminals of a single neuron. *Nature.* 392:82–86. https://doi.org/10.1038/32176

Davis, G.W., and M. Müller. 2015. Homeostatic control of presynaptic neurotransmitter release. *Annu. Rev. Physiol.* 77:251–270. https://doi.org/10.1146/annurev-physiol-021014-071740

Dickman, D.K., and G.W. Davis. 2009. The schizophrenia susceptibility gene dysbindin controls synaptic homeostasis. *Science.* 326:1127–1130. https://doi.org/10.1126/science.1179685

Dickman, D.K., J.A. Horne, I.A. Meinertzhagen, and T.L. Schwarz. 2005. A slowed classical pathway rather than kiss-and-run mediates endocytosis at synapses lacking synaptojanin and endophilin. *Cell.* 123:521–533. https://doi.org/10.1016/j.cell.2005.09.026

Dickman, D.K., Z. Lu, I.A. Meinertzhagen, and T.L. Schwarz. 2006. Altered synaptic development and active zone spacing in endocytosis mutants. *Curr. Biol.* 16:591–598. https://doi.org/10.1016/j.cub.2006.02.058

Diering, G.H., R.S. Nirujogi, R.H. Roth, P.F. Worley, A. Pandey, and R.L. Huganir. 2017. Homer1a drives homeostatic scaling-down of excitatory synapses during sleep. *Science.* 355:511–515. https://doi.org/10.1126/science.aai8355

Dong, W., T. Radulovic, R.O. Goral, C. Thomas, M. Suarez Montesinos, D. Guerrero-Given, A. Hagiwara, T. Putzke, Y. Hida, M. Abe, et al. 2018. CAST/ELKS Proteins Control Voltage-Gated Ca^{2+} Channel Density and Synaptic Release Probability at a Mammalian Central Synapse. *Cell Reports.* 24:284–293.e6. https://doi.org/10.1016/j.celrep.2018.06.024

Ehmann, N., S. van de Linde, A. Alon, D. Ljaschenko, X.Z. Keung, T. Holm, A. Rings, A. DiAntonio, S. Hallermann, U. Ashery, et al. 2014. Quantitative super-resolution imaging of Bruchpilot distinguishes active zone states. *Nat. Commun.* 5:4650. https://doi.org/10.1038/ncomms5650

Eichler, S.A., and J.C. Meier. 2008. E-I balance and human diseases - from molecules to networking. *Front. Mol. Neurosci.* 1:2. https://doi.org/10.3389/neuro.02.002.2008

Frank, C.A. 2014. Homeostatic plasticity at the Drosophila neuromuscular junction. *Neuropharmacology.* 78:63–74. https://doi.org/10.1016/j.neuropharm.2013.06.015

Frank, C.A., M.J. Kennedy, C.P. Goold, K.W. Marek, and G.W. Davis. 2006. Mechanisms underlying the rapid induction and sustained expression of synaptic homeostasis. *Neuron.* 52:663–677. https://doi.org/10.1016/j.neuron.2006.09.029

Gaviño, M.A., K.J. Ford, S. Archila, and G.W. Davis. 2015. Homeostatic synaptic depression is achieved through a regulated decrease in presynaptic calcium channel abundance. *eLife.* 4:e05473. https://doi.org/10.7554/eLife.05473

Glebov, O.O., R.E. Jackson, C.M. Winterflood, D.M. Owen, E.A. Barker, P. Doherty, H. Ewers, and J. Burrone. 2017. Nanoscale Structural Plasticity of the Active Zone Matrix Modulates Presynaptic Function. *Cell Reports.* 18:2715–2728. https://doi.org/10.1016/j.celrep.2017.02.064

Goel, P., and D. Dickman. 2018. Distinct homeostatic modulations stabilize reduced postsynaptic receptivity in response to presynaptic DLK signaling. *Nat. Commun.* 9:1856. https://doi.org/10.1038/s41467-018-04270-0

Goel, P., X. Li, and D. Dickman. 2017. Disparate Postsynaptic Induction Mechanisms Ultimately Converge to Drive the Retrograde Enhancement of Presynaptic Efficacy. *Cell Reports.* 21:2339–2347. https://doi.org/10.1016/j.celrep.2017.10.116

Goel, P., M. Khan, S. Howard, G. Kim, B. Kiragasi, K. Kikuma, and D. Dickman. 2019a. A screen for synaptic growth mutants reveals mechanisms that stabilize synaptic strength. *J. Neurosci.* https://doi.org/10.1523/JNEUROSCI.2601-18.2019

Goel, P., X. Li, and D. Dickman. 2019b. Estimation of the Readily Releasable Synaptic Vesicle Pool at the *Drosophila* Larval Neuromuscular Junction. *Bio Protoc.* 9:e3127. https://doi.org/10.21769/BioProtoc.3127

Graf, E.R., R.W. Daniels, R.W. Burgess, T.L. Schwarz, and A. DiAntonio. 2009. Rab3 dynamically controls protein composition at active zones. *Neuron.* 64:663–677. https://doi.org/10.1016/j.neuron.2009.11.002

Gratz, S.J., P. Goel, J.J. Bruckner, R.X. Hernandez, K. Khateeb, G.T. Macleod, D. Dickman, and K.M. O'Connor-Giles. 2019. Endogenous tagging reveals differential regulation of Ca^{2+} channels at single AZs during presynaptic homeostatic potentiation and depression. *J. Neurosci.* 28:3068–3018.

Grillo, F.W., G. Neves, A. Walker, G. Vizcay-Barrena, R.A. Fleck, T. Branco, and J. Burrone. 2018. A Distance-Dependent Distribution of Presynaptic Boutons Tunes Frequency-Dependent Dendritic Integration. *Neuron.* 99:275–282.e3. https://doi.org/10.1016/j.neuron.2018.06.015

Guerrero, G., D.F. Reiff, G. Agarwal, R.W. Ball, A. Borst, C.S. Goodman, and E.Y. Isacoff. 2005. Heterogeneity in synaptic transmission along a Drosophila larval motor axon. *Nat. Neurosci.* 8:1188–1196. https://doi.org/10.1038/nn1526

Hauswirth, A.G., K.J. Ford, T. Wang, R.D. Fetter, A. Tong, and G.W. Davis. 2018. A postsynaptic PI3K-cII dependent signaling controller for presynaptic homeostatic plasticity. *eLife.* 7:e31535. https://doi.org/10.7554/eLife.31535

Hengen, K.B., A. Torrado Pacheco, J.N. McGregor, S.D. Van Hooser, and G.G. Turrigiano. 2016. Neuronal Firing Rate Homeostasis Is Inhibited by Sleep and Promoted by Wake. *Cell.* 165:180–191. https://doi.org/10.1016/j.cell.2016.01.046

Herring, B.E., and R.A. Nicoll. 2016. Long-Term Potentiation: From CaMKII to AMPA Receptor Trafficking. *Annu. Rev. Physiol.* 78:351–365. https://doi.org/10.1146/annurev-physiol-021014-071753

Holderith, N., A. Lorincz, G. Katona, B. Rózsa, A. Kulik, M. Watanabe, and Z. Nusser. 2012. Release probability of hippocampal glutamatergic terminals scales with the size of the active zone. *Nat. Neurosci.* 15:988–997. https://doi.org/10.1038/nn.3137

Holtmaat, A., and K. Svoboda. 2009. Experience-dependent structural synaptic plasticity in the mammalian brain. *Nat. Rev. Neurosci.* 10:647–658. https://doi.org/10.1038/nrn2699

Hou, Q., J. Gilbert, and H.Y. Man. 2011. Homeostatic regulation of AMPA receptor trafficking and degradation by light-controlled single-synaptic activation. *Neuron.* 72:806–818. https://doi.org/10.1016/j.neuron.2011.10.011

Hruska, M., N. Henderson, S.J. Le Marchand, H. Jafri, and M.B. Dalva. 2018. Synaptic nanomodules underlie the organization and plasticity of spine synapses. *Nat. Neurosci.* 21:671–682. https://doi.org/10.1038/s41593-018-0138-9

Hunt, M.J., N.J. Kopell, R.D. Traub, and M.A. Whittington. 2017. Aberrant Network Activity in Schizophrenia. *Trends Neurosci.* 40:371–382. https://doi.org/10.1016/j.tins.2017.04.003

Keck, T., M. Hübener, and T. Bonhoeffer. 2017. Interactions between synaptic homeostatic mechanisms: an attempt to reconcile BCM theory, synaptic scaling, and changing excitation/inhibition balance. *Curr. Opin. Neurobiol.* 43:87–93. https://doi.org/10.1016/j.conb.2017.02.003

Kikuma, K., X. Li, D. Kim, D. Sutter, and D.K. Dickman. 2017. Extended Synaptotagmin Localizes to Presynaptic ER and Promotes Neurotransmission and Synaptic Growth in *Drosophila*. *Genetics.* 207:993–1006. https://doi.org/10.1534/genetics.117.300261

Kikuma, K., X. Li, S. Perry, Q. Li, P. Goel, C. Chen, D. Kim, N. Stavropoulos, and D. Dickman. 2018. The sleep gene insomniac ubiquitinates targets at postsynaptic densities and is required for retrograde homeostatic signaling. *bioRxiv.* doi:10.1101/430819 (Preprint posted September 29, 2018)

Kiragasi, B., J. Wondolowski, Y. Li, and D.K. Dickman. 2017. A Presynaptic Glutamate Receptor Subunit Confers Robustness to Neurotransmission and Homeostatic Potentiation. *Cell Reports.* 19:2694–2706. https://doi.org/10.1016/j.celrep.2017.06.003

Kittel, R.J., C. Wichmann, T.M. Rasse, W. Fouquet, M. Schmidt, A. Schmid, D.A. Wagh, C. Pawlu, R.R. Kellner, K.I. Willig, et al. 2006. Bruchpilot promotes active zone assembly, Ca2+ channel clustering, and vesicle release. *Science.* 312:1051–1054. https://doi.org/10.1126/science.1126308

Koh, T.W., P. Verstreken, and H.J. Bellen. 2004. Dap160/intersectin acts as a stabilizing scaffold required for synaptic development and vesicle endocytosis. *Neuron.* 43:193–205. https://doi.org/10.1016/j.neuron.2004.06.029

Landau, I.D., R. Egger, V.J. Dercksen, M. Oberlaender, and H. Sompolinsky. 2016. The Impact of Structural Heterogeneity on Excitation-Inhibition Balance in Cortical Networks. *Neuron.* 92:1106–1121. https://doi.org/10.1016/j.neuron.2016.10.027

Li, X., P. Goel, C. Chen, V. Angajala, X. Chen, and D.K. Dickman. 2018a. Synapse-specific and compartmentalized expression of presynaptic homeostatic potentiation. *eLife.* 7:e34338. https://doi.org/10.7554/eLife.34338

Li, X., P. Goel, J. Wondolowski, J. Paluch, and D. Dickman. 2018b. A Glutamate Homeostat Controls the Presynaptic Inhibition of Neurotransmitter Release. *Cell Reports.* 23:1716–1727. https://doi.org/10.1016/j.celrep.2018.03.130

Liebl, F.L., K.M. Werner, Q. Sheng, J.E. Karr, B.D. McCabe, and D.E. Featherstone. 2006. Genome-wide P-element screen for Drosophila synaptogenesis mutants. *J. Neurobiol.* 66:332–347. https://doi.org/10.1002/neu.20229

Lübbert, M., R.O. Goral, C. Keine, C. Thomas, D. Guerrero-Given, T. Putzke, R. Satterfield, N. Kamasawa, and S.M.J. Young Jr. 2019. $Ca_V2.1$ α_1 Subunit Expression Regulates Presynaptic $Ca_V2.1$ Abundance and Synaptic Strength at a Central Synapse. *Neuron.* 101:260–273.e6. https://doi.org/10.1016/j.neuron.2018.11.028

Mackler, J.M., J.A. Drummond, C.A. Loewen, I.M. Robinson, and N.E. Reist. 2002. The C(2)B Ca(2+)-binding motif of synaptotagmin is required for synaptic transmission in vivo. *Nature.* 418:340–344. https://doi.org/10.1038/nature00846

Maglione, M., and S.J. Sigrist. 2013. Seeing the forest tree by tree: super-resolution light microscopy meets the neurosciences. *Nat. Neurosci.* 16:790–797. https://doi.org/10.1038/nn.3403

Mahr, A., and H. Aberle. 2006. The expression pattern of the Drosophila vesicular glutamate transporter: a marker protein for motoneurons and glutamatergic centers in the brain. *Gene Expr. Patterns.* 6:299–309. https://doi.org/10.1016/j.modgep.2005.07.006

Marie, B., S.T. Sweeney, K.E. Poskanzer, J. Roos, R.B. Kelly, and G.W. Davis. 2004. Dap160/intersectin scaffolds the periactive zone to achieve high-fidelity endocytosis and normal synaptic growth. *Neuron.* 43:207–219. https://doi.org/10.1016/j.neuron.2004.07.001

Marrus, S.B., and A. DiAntonio. 2004. Preferential localization of glutamate receptors opposite sites of high presynaptic release. *Curr. Biol.* 14: 924–931. https://doi.org/10.1016/j.cub.2004.05.047

Matkovic, T., M. Siebert, E. Knoche, H. Depner, S. Mertel, D. Owald, M. Schmidt, U. Thomas, A. Sickmann, D. Kamin, et al. 2013. The Bruchpilot cytomatrix determines the size of the readily releasable pool of synaptic vesicles. *J. Cell Biol.* 202:667–683. https://doi.org/10.1083/jcb.201301072

Matsuzaki, M., N. Honkura, G.C. Ellis-Davies, and H. Kasai. 2004. Structural basis of long-term potentiation in single dendritic spines. *Nature.* 429: 761–766. https://doi.org/10.1038/nature02617

Matz, J., A. Gilyan, A. Kolar, T. McCarvill, and S.R. Krueger. 2010. Rapid structural alterations of the active zone lead to sustained changes in neurotransmitter release. *Proc. Natl. Acad. Sci. USA.* 107:8836–8841. https://doi.org/10.1073/pnas.0906087107

Melom, J.E., Y. Akbergenova, J.P. Gavornik, and J.T. Littleton. 2013. Spontaneous and evoked release are independently regulated at individual active zones. *J. Neurosci.* 33:17253–17263. https://doi.org/10.1523/JNEUROSCI.3334-13.2013

Menon, K.P., R.A. Carrillo, and K. Zinn. 2013. Development and plasticity of the Drosophila larval neuromuscular junction. *Wiley Interdiscip. Rev. Dev. Biol.* 2:647–670. https://doi.org/10.1002/wdev.108

Miller, D.L., S.L. Ballard, and B. Ganetzky. 2012. Analysis of synaptic growth and function in Drosophila with an extended larval stage. *J. Neurosci.* 32: 13776–13786. https://doi.org/10.1523/JNEUROSCI.0508-12.2012

Müller, M., and G.W. Davis. 2012. Transsynaptic control of presynaptic Ca^{2+} influx achieves homeostatic potentiation of neurotransmitter release. *Curr. Biol.* 22:1102–1108. https://doi.org/10.1016/j.cub.2012.04.018

Müller, M., E.C. Pym, A. Tong, and G.W. Davis. 2011. Rab3-GAP controls the progression of synaptic homeostasis at a late stage of vesicle release. *Neuron.* 69:749–762. https://doi.org/10.1016/j.neuron.2011.01.025

Murthy, V.N., T. Schikorski, C.F. Stevens, and Y. Zhu. 2001. Inactivity produces increases in neurotransmitter release and synapse size. *Neuron.* 32:673–682. https://doi.org/10.1016/S0896-6273(01)00500-1

Nagarkar-Jaiswal, S., P.T. Lee, M.E. Campbell, K. Chen, S. Anguiano-Zarate, M.C. Gutierrez, T. Busby, W.W. Lin, Y. He, K.L. Schulze, et al. 2015. A library of MiMICs allows tagging of genes and reversible, spatial and temporal knockdown of proteins in Drosophila. *eLife.* 4:e05338. https://doi.org/10.7554/eLife.05338

Nelson, S.B., and V. Valakh. 2015. Excitatory/Inhibitory Balance and Circuit Homeostasis in Autism Spectrum Disorders. *Neuron.* 87:684–698. https://doi.org/10.1016/j.neuron.2015.07.033

Newman, Z.L., A. Hoagland, K. Aghi, K. Worden, S.L. Levy, J.H. Son, L.P. Lee, and E.Y. Isacoff. 2017. Input-Specific Plasticity and Homeostasis at the Drosophila Larval Neuromuscular Junction. *Neuron.* 93:1388–1404.e10. https://doi.org/10.1016/j.neuron.2017.02.028

O'Connor-Giles, K.M., L.L. Ho, and B. Ganetzky. 2008. Nervous wreck interacts with thickveins and the endocytic machinery to attenuate retrograde BMP signaling during synaptic growth. *Neuron.* 58:507–518. https://doi.org/10.1016/j.neuron.2008.03.007

Paradis, S., S.T. Sweeney, and G.W. Davis. 2001. Homeostatic control of presynaptic release is triggered by postsynaptic membrane depolarization. *Neuron.* 30:737–749. https://doi.org/10.1016/S0896-6273(01)00326-9

Paul, M.M., M. Pauli, N. Ehmann, S. Hallermann, M. Sauer, R.J. Kittel, and M. Heckmann. 2015. Bruchpilot and Synaptotagmin collaborate to drive rapid glutamate release and active zone differentiation. *Front. Cell. Neurosci.* 9:29. https://doi.org/10.3389/fncel.2015.00029

Peled, E.S., and E.Y. Isacoff. 2011. Optical quantal analysis of synaptic transmission in wild-type and rab3-mutant Drosophila motor axons. *Nat. Neurosci.* 14:519–526. https://doi.org/10.1038/nn.2767

Perry, S., Y. Han, A. Das, and D. Dickman. 2017. Homeostatic plasticity can be induced and expressed to restore synaptic strength at neuromuscular junctions undergoing ALS-related degeneration. *Hum. Mol. Genet.* 26: 4153–4167. https://doi.org/10.1093/hmg/ddx304

Petersen, S.A., R.D. Fetter, J.N. Noordermeer, C.S. Goodman, and A. DiAntonio. 1997. Genetic analysis of glutamate receptors in Drosophila reveals a retrograde signal regulating presynaptic transmitter release. *Neuron.* 19:1237–1248. https://doi.org/10.1016/S0896-6273(00)80415-8

Pozo, K., and Y. Goda. 2010. Unraveling mechanisms of homeostatic synaptic plasticity. *Neuron.* 66:337–351. https://doi.org/10.1016/j.neuron.2010.04.028

Reddy-Alla, S., M.A. Böhme, E. Reynolds, C. Beis, A.T. Grasskamp, M.M. Mampell, M. Maglione, M. Jusyte, U. Rey, H. Babikir, et al. 2017. Stable Positioning of Unc13 Restricts Synaptic Vesicle Fusion to Defined Release Sites to Promote Synchronous Neurotransmission. *Neuron.* 95: 1350–1364.e12. https://doi.org/10.1016/j.neuron.2017.08.016

Rushton, E., J. Rohrbough, and K. Broadie. 2009. Presynaptic secretion of mind-the-gap organizes the synaptic extracellular matrix-integrin interface and postsynaptic environments. *Dev. Dyn.* 238:554–571. https://doi.org/10.1002/dvdy.21864

Schuster, C.M., G.W. Davis, R.D. Fetter, and C.S. Goodman. 1996. Genetic dissection of structural and functional components of synaptic plasticity. II. Fasciclin II controls presynaptic structural plasticity. *Neuron.* 17:655–667. https://doi.org/10.1016/S0896-6273(00)80198-1

Stewart, B.A., H.L. Atwood, J.J. Renger, J. Wang, and C.F. Wu. 1994. Improved stability of Drosophila larval neuromuscular preparations in haemolymph-like physiological solutions. *J. Comp. Physiol. A Neuroethol. Sens. Neural Behav. Physiol.* 175:179–191. https://doi.org/10.1007/BF00215114

Styr, B., and I. Slutsky. 2018. Imbalance between firing homeostasis and synaptic plasticity drives early-phase Alzheimer's disease. *Nat. Neurosci.* 21:463–473. https://doi.org/10.1038/s41593-018-0080-x

Tang, A.H., H. Chen, T.P. Li, S.R. Metzbower, H.D. MacGillavry, and T.A. Blanpied. 2016. A trans-synaptic nanocolumn aligns neurotransmitter release to receptors. *Nature.* 536:210–214. https://doi.org/10.1038/nature19058

Tokuoka, H., and Y. Goda. 2008. Activity-dependent coordination of presynaptic release probability and postsynaptic GluR2 abundance at single synapses. *Proc. Natl. Acad. Sci. USA.* 105:14656–14661. https://doi.org/10.1073/pnas.0805705105

Turrigiano, G. 2012. Homeostatic synaptic plasticity: local and global mechanisms for stabilizing neuronal function. *Cold Spring Harb. Perspect. Biol.* 4:a005736. https://doi.org/10.1101/cshperspect.a005736

Turrigiano, G.G., and S.B. Nelson. 2004. Homeostatic plasticity in the developing nervous system. *Nat. Rev. Neurosci.* 5:97–107. https://doi.org/10.1038/nrn1327

Turrigiano, G.G., K.R. Leslie, N.S. Desai, L.C. Rutherford, and S.B. Nelson. 1998. Activity-dependent scaling of quantal amplitude in neocortical neurons. *Nature.* 391:892–896. https://doi.org/10.1038/36103

Van Vactor, D., and S.J. Sigrist. 2017. Presynaptic morphogenesis, active zone organization and structural plasticity in Drosophila. *Curr. Opin. Neurobiol.* 43:119–129. https://doi.org/10.1016/j.conb.2017.03.003

Verstreken, P., O. Kjaerulff, T.E. Lloyd, R. Atkinson, Y. Zhou, I.A. Meinertzhagen, and H.J. Bellen. 2002. Endophilin mutations block clathrin-mediated endocytosis but not neurotransmitter release. *Cell.* 109: 101–112. https://doi.org/10.1016/S0092-8674(02)00688-8

Vukoja, A., U. Rey, A.G. Petzoldt, C. Ott, D. Vollweiter, C. Quentin, D. Puchkov, E. Reynolds, M. Lehmann, S. Hohensee, et al. 2018. Presynaptic Biogenesis Requires Axonal Transport of Lysosome-Related Vesicles. *Neuron.* 99:1216–1232.e7. https://doi.org/10.1016/j.neuron.2018.08.004

Wagh, D.A., T.M. Rasse, E. Asan, A. Hofbauer, I. Schwenkert, H. Dürrbeck, S. Buchner, M.C. Dabauvalle, M. Schmidt, G. Qin, et al. 2006. Bruchpilot, a protein with homology to ELKS/CAST, is required for structural integrity and function of synaptic active zones in Drosophila. *Neuron.* 49: 833–844. https://doi.org/10.1016/j.neuron.2006.02.008

Wentzel, C., I. Delvendahl, S. Sydlik, O. Georgiev, and M. Müller. 2018. Dysbindin links presynaptic proteasome function to homeostatic recruitment of low release probability vesicles. *Nat. Commun.* 9:267. https://doi.org/10.1038/s41467-017-02494-0

Weyhersmüller, A., S. Hallermann, N. Wagner, and J. Eilers. 2011. Rapid active zone remodeling during synaptic plasticity. *J. Neurosci.* 31: 6041–6052. https://doi.org/10.1523/JNEUROSCI.6698-10.2011

Yizhar, O., L.E. Fenno, M. Prigge, F. Schneider, T.J. Davidson, D.J. O'Shea, V.S. Sohal, I. Goshen, J. Finkelstein, J.T. Paz, et al. 2011. Neocortical excitation/inhibition balance in information processing and social dysfunction. *Nature.* 477:171–178. https://doi.org/10.1038/nature10360